



Novel complexes with ONNO tetradentate coumarin schiff-base donor ligands: x-ray structures, DFT calculations, molecular dynamics and potential anticarcinogenic activity

Paula Daniela Mestizo · Diana M. Narváez · Jesús Alberto Pinzón-Ulloa · Daniela Torres Di Bello · Sebastian Franco-Ulloa · Mario A. Macías · Helena Groot · Gian Pietro Miscione · Leopoldo Suescun · John J. Hurtado 

Received: 27 August 2020 / Accepted: 4 November 2020
© Springer Nature B.V. 2020

Abstract The synthesis of eight novel Zn(II), Co(II), Cu(II), Ni(II) and Pt(II) complexes (**2–9**) derived from the ONNO tetradentate coumarin Schiff-Base donor ligands, **L**₁ and the novel **L**₂, was performed. All compounds were characterized by analytical, spectrometry and spectroscopy techniques. Complexes **2–4** were also characterized by DFT calculations and the structures of **5** and **6** were determined by single-crystal X-ray diffraction analysis. A cytotoxicity study was carried out through an

MTT assay in the carcinogenic cell line HeLa and the noncarcinogenic cell lines HFF-1 and HaCaT. The results indicated that among all the evaluated compounds, **2** and **6** presented the best anticarcinogenic potential against HeLa cells with an IC₅₀ of 3.5 and 4.1 μM, respectively. In addition, classical molecular dynamics simulations were performed on the synthesized coordination compounds bound to G4 DNA architectures in the scope of shedding light on their inhibition mode and the most conserved interactions that may lead to the biological activity of the compounds.

Electronic supplementary material The online version of this article (<https://doi.org/10.1007/s10534-020-00268-8>) contains supplementary material, which is available to authorized users.

P. D. Mestizo · M. A. Macías · J. J. Hurtado (✉)
Departamento de Química, Universidad de Los Andes,
Carrera 1 No. 18A-12, 111711 Bogotá, Colombia
e-mail: jj.hurtado@uniandes.edu.co

D. M. Narváez · J. A. Pinzón-Ulloa ·
D. T. Di Bello · H. Groot
Human Genetics Laboratory, Universidad de Los Andes,
Carrera 1 No. 18A-12, 111711 Bogotá, Colombia

S. Franco-Ulloa · G. P. Miscione
COBO Computational Bio-Organic Chemistry, Chemistry
Department, Universidad de Los Andes, Carrera 1 No.
18A-12, 111711 Bogotá, Colombia

L. Suescun
Cryssmat-Lab/Cátedra de Física/DETEMA, Facultad de
Química, Universidad de La República, Montevideo,
Uruguay

Keywords Bioinorganic chemistry · Anticarcinogenic activity · Coumarin schiff base ligands · G-quadruplex DNA · Structure elucidation

Introduction

According to the World Health Organization, cancer is an important cause of mortality, leaving an estimated 9.6 million deaths and 18.1 million new cases in 2018 (Bray et al. 2018). Chemotherapy is one of the classic treatments used for this disease, in addition to surgical excision and irradiation (Robillard and Reedijk 2011). Among several organic and inorganic compounds, cisplatin and its derivatives are commonly used chemotherapeutic agents that are effective against a wide variety of tumors of high

medical importance (Mehmood 2014). Nevertheless, it is also well known that these drugs have developed resistance and a series of secondary effects due to their lack of selectivity for a specific molecular target (Robillard and Reedijk 2011; Mehmood 2014). Consequently, the design of new metal complexes as selective and effective anticancer drugs continues to be of great interest to the scientific community (Hartinger et al. 2008; Voulgari et al. 2016).

Recently, ONNO donor complexes containing Schiff bases, such as the salphen complexes (**A–D**) presented in Fig. 1a, have emerged as selective and effective anticarcinogenic compounds (Reed et al. 2006; Wu et al. 2009; Campbell et al. 2012). Their selectivity is attributed to the proposed mechanism of action, which involves the stabilization of a convenient molecular target known as G-quadruplex DNA (G4) (Cao et al. 2017). G4 consists of stacked guanine quartets (GCs) (Fig. 1b) stabilized by a tunnel of cationic metals (e.g. Na^+ and K^+) (Fig. 1c) and is found in critical genomic zones such as telomeres and oncogene promoters (e.g. NHE III of

the *cMyc* oncogene, overexpressed in 80% of the solid tumors) (Mendoza et al. 2016). Therefore, the stabilization of G4 can inhibit important biological processes such as the cellular transcription in these specific zones (Burge et al. 2006; Wu et al. 2009; Ma et al. 2013; Abd Karim et al. 2014; David et al. 2016; Mendoza et al. 2016). Additionally, empirical data suggest that cancer genomes contain more G4 structures than normal cell genomes, which confers more specificity for the inhibition of cellular processes in cancer cells on G4 stabilizers (Hänsel-Hertsch et al. 2017).

Salphen complexes may act as G4 stabilizers since they present two main structural features. The first one consists of a delocalized π -electron cloud which is intrinsically present in the ligand and can be easily modified to achieve a better π -stacking interaction with the G4 structure (Reed et al. 2006). The second feature is the chosen metallic center, as it typically confers a square-planar or square pyramidal geometry which facilitates the π -stacking interaction of the ligand with the G4 structure (Campbell et al. 2012).

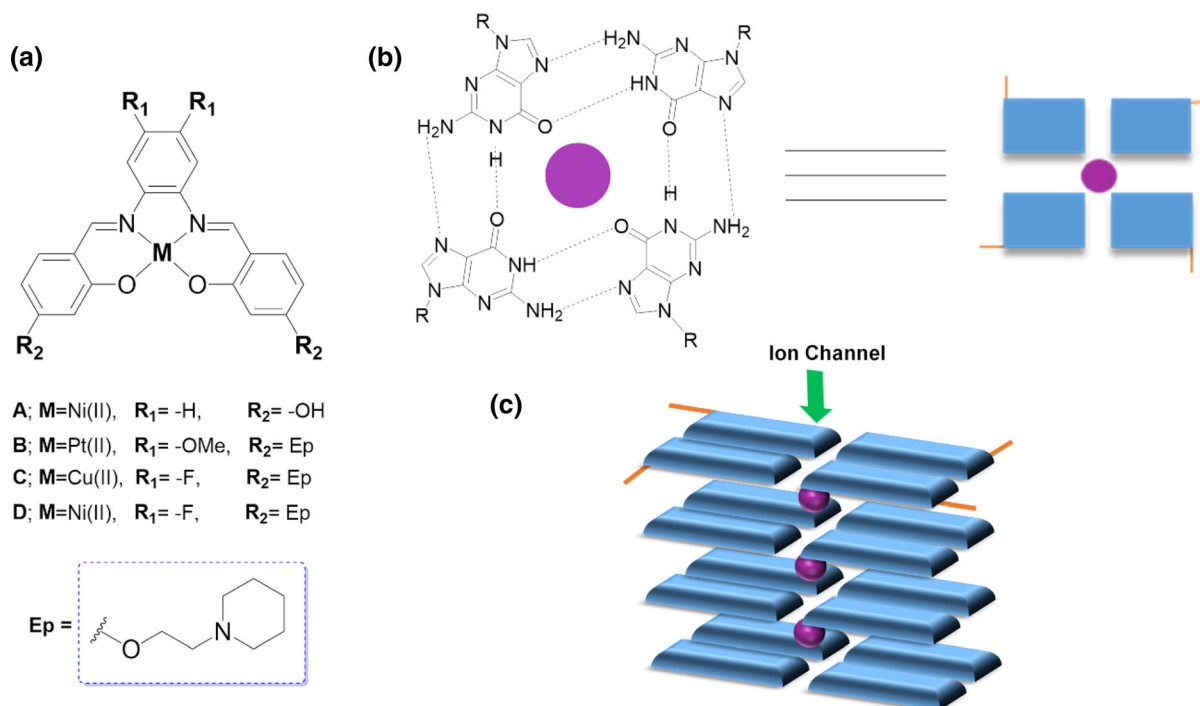


Fig. 1 a Salphen metal complexes used as G4 stabilizers with anticarcinogenic potential (Reed et al. 2006; Wu et al. 2009; Campbell et al. 2012). General G4 structure. b Guanine quartet (GC) graphical representation and c Stacked GCs that form the

G4 structure (DNA binding represented as orange lines and metallic cations represented as purple spheres. (Color figure online))

Moreover, the cation metal can also function as an ion stabilizer in the top/end of the GCs tunnel (Campbell et al. 2012).

In the present work, we report the synthesis and characterization of eight novel Zn(II), Co(II), Cu(II), Ni(II) and Pt(II) metal complexes containing the coumarin salphen-like ligands L_1 (Nuñez-Dallos et al. 2016) and the novel L_2 . These salphen-like ligands contain coumarin moieties, which are known to exhibit anticarcinogenic activity (Hassan et al. 2018) and also cause a high π -electronic delocalization of the overall ligand. We aimed to explore the structural features of the ligands with regard to the potential anticarcinogenic activity of the complexes. Furthermore, preliminary research on the potential mechanism of action of the complexes under study related to the stabilization of the G4 structure was carried out using molecular dynamics (MD) calculations.

Experimental

Materials and methods

Chemical studies

All reagents (cobalt(II) acetate tetrahydrate, copper (II) acetate monohydrate, nickel acetate tetrahydrate, zinc acetate dihydrate, sodium acetate, Pd/C (10 wt %) and K_2PtCl_4) were purchased from Alfa Aesar or Sigma Aldrich and used without further purification. All solvents used were ACS-grade and obtained from PanReac AppliChem. The synthetic procedures for the previously reported ligand 8,8'-((1E,1'E)-(1,2-phenylenebis(azaneylylidene))bis(methaneylylidene))bis(7-hydroxy-2H-chromen-2-one) (L_1), complex 8,8'-((1E,1'E)-(1,2-phenylenebis(azaneylylidene))bis(methaneylylidene))bis(7-hydroxy-2H-chromen-2-one)zinc(II) (**1**) and the 8-formyl-7-hydroxycoumarin precursor are shown in the electronic supplementary information (ESI) section (Nuñez-Dallos et al. 2016).

1H NMR and ^{13}C NMR were performed on a Bruker Advance III HD Ascend 400 spectrometer (400.13 MHz for 1H ; 100.61 MHz for ^{13}C). Chemical shifts (δ) are reported in parts per million (ppm) relative to TMS or the residual signals of the deuterated solvents ($CDCl_3$: 1H NMR δ : 7.26 and

^{13}C NMR δ : 77.2; $DMSO-d_6$: 1H NMR δ : 2.50 and ^{13}C NMR δ : 39.5). High resolution mass spectra (HRMS) were recorded on an Agilent Technologies Q-TOF 6520 spectrometer with electrospray ionization (ESI) in positive ion mode. Fourier transform infrared (FTIR) spectra were obtained on a Shimadzu IR Tracer-100 spectrometer using a single-reflection ATR accessory. Raman spectra were acquired on a HORIBA Scientific apparatus in the range between 150 and 1750 cm^{-1} . UV-Vis spectra were measured on a Variant Cary 100 spectrophotometer (Agilent Technologies) from 200 to 800 nm in a quartz cuvette with a path length of 1 cm. Fluorescence spectra were recorded using an Agilent Cary Eclipse spectrometer in the range between 200 and 700 nm. Thermogravimetric analysis (TGA) of the complexes were carried out on a TGA 55 instrument (TA Instruments) under a nitrogen atmosphere with a continuous flow of 100 mL/min. The samples were heated from 25 to 700 °C with a heating rate of 10 °C/min. Elemental analysis (C, H and N) was performed with a Thermo Scientific FLASH 2000 CHNS/O analyzer. Melting points were reported uncorrected and were determined in open capillary tubes on a Mel-Temp electrothermal melting point apparatus.

Biological studies

Cisplatin was purchased from Sigma Aldrich and used without further purification. The human cervical epithelioid carcinoma cell line HeLa (ATCC CCL-2), the human foreskin fibroblast cell line HFF-1 (ATCC SCRC-1041), and the human keratinocyte cell line HaCaT were grown as monolayers and maintained in Dulbecco's modified Eagle's medium (DMEM) purchased from Sigma Aldrich. Culture media were supplemented with 10% and 15% fetal bovine serum (FBS) (for HeLa and HaCaT cells and HFF-1 cells, respectively), 1% penicillin/streptomycin and 2% glutamine all of which were purchased from GIBCO. The cultures were incubated at 37 °C under a humidified 5% CO_2 atmosphere for two complete cell cycles (24 h) before treatment. 3-(4,5-Dimethylthiazol-2,5-diphenyl)tetrazolium bromide (MTT) was also obtained from Sigma Aldrich. The MTT-formazan absorption was measured on a Bio-Rad Model 680 microplate reader with detection in UV-Vis range.

Synthesis of L2 and complexes 2–9

Synthesis of 8,8'-((1E,1'E)-((4,5-dimethoxy-1,2-phenylene)bis(azaneylylidene))bis(methaneylylidene))bis(7-hydroxy-2H-chromen-2-one) (L2)

A solution of 1,2-dimethoxy-4,5-diaminebenzene (0.139 g, 0.824 mmol) in ethanol (EtOH) (15 mL) was added to a stirred solution of 8-formyl-7-hydroxycoumarin (0.313 g, 1.646 mmol) in the same solvent (25 mL). The reaction mixture was refluxed for 2 h. The resulting solid was filtered and washed with portions of cold EtOH (9 × 10 mL) and diethyl ether (1 × 10 mL) to yield the product as an orange solid. Yield: 0.333 g (78%). M.p.: 261–263 °C. ATR FTIR (podwer, cm⁻¹): ν 3591w, 3460w, 3062vw, 3005vw, 2939vw, 1743vs, 1716vs, 1612vs, 1508vs, 1462 s, 1404w, 1354w, 1311w, 1269 s, 1238 s, 1188w, 1157w, 1122 s, 1010 s, 918w. Raman (cm⁻¹): 227, 341, 379, 407, 469, 545, 629, 658, 770, 912, 972, 1004, 11,048, 1179, 1201, 1264, 1337, 1396, 1448, 1574. Anal. Calcd. For C₂₈H₂₀N₂O₈·1.3 H₂O: C, 62.80; H, 4.25; N, 5.23%. Found: C, 62.83; H, 4.15; N, 5.74%. ¹H NMR (400 MHz, CDCl₃) δ 14.86 (s, 2H), 9.32 (s, 2H), 7.65 (d, *J*=9.5 Hz, 2H), 7.43 (d, *J*=8.8 Hz, 2H), 6.94 (d, *J*=8.8 Hz, 2H), 6.92 (s, 2H), 6.25 (d, *J*=9.5 Hz, 2H), 4.04 (s, 6H). ¹³C NMR (100 MHz, CDCl₃) δ 166.7, 160.5, 155.2, 150.0, 144.3, 134.3, 132.6, 115.7, 112.1, 110.3, 107.4, 102.5. HRMS (ESI+) *m/z* Calcd. For [C₂₈H₂₀N₂O₈+H]⁺: 513.1298. Found: 513.1294 [M+H]⁺. UV–Vis (0.01 mM; dimethyl sulfoxide (DMSO)) λ_{\max} , nm (Log ϵ , M⁻¹ cm⁻¹): 333 (4.62), 258 (4.53).

Synthesis of complexes 2–8

The general synthesis of complexes **2–8** containing Zn(II), Co(II), Cu(II) and Ni(II) metal centers is described as follows (for specific synthetic details refer to the ESI section). A solution of a slight excess of the hydrate of the respective metal acetate M(OAc)₂ in EtOH was added to a suspension of the ligand (L₁ or L₂) in dichloromethane (DCM) (stoichiometric ratio 1.1: 1.0; M(OAc)₂: ligand). The mixture was refluxed for 2 to 4 h depending on the ligand. The solvent was evaporated to dryness and the resulting solid was with different solvents such as EtOH, ethyl acetate and diethyl ether.

8,8'-((1E,1'E)-(1,2-phenylenebis(azaneylylidene))bis(methaneylylidene))bis(7-hydroxy-2H-chromen-2-one)cobalt(II) (2) Yield: 0.076 g (66%). M.p.: > 400 °C. ATR FTIR (podwer, cm⁻¹): ν 3560vw, 3093vw, 2958vw, 2924vw, 2839vw, 1728vs, 1620 s, 1578vs, 1519 s, 1489w, 1462 m, 1408w, 1354 s, 1253w, 1226w, 1203w, 1157w, 1103 s, 1002 m, 829vs, 771 s, 752 s. Raman (cm⁻¹): 264w, 300w, 383w, 434w, 464vw, 503w, 538wv, 628vw, 723w, 896vw, 930vw, 992vw, 1038vw, 1073vw, 1097w, 1142w, 1169w, 1214 m, 1275w, 1359 s, 1406 s, 1441w, 1511w, 1559vs. Anal. Calcd. For C₂₆H₁₆CoN₂O₇: C, 59.22; H, 3.06; N, 5.31%. Found: C, 58.67; H, 2.80; N, 4.86%. UV–Vis (0.017 mM; chloroform (CHCl₃)) λ_{\max} , nm (Log ϵ , M⁻¹ cm⁻¹): 350 (4.69), 435 (4.24), 535 (3.70), 578 (3.39).

8,8'-((1E,1'E)-(1,2-phenylenebis(azaneylylidene))bis(methaneylylidene))bis(7-hydroxy-2H-chromen-2-one)copper(II) (3) Yield: 0.083 g (71%). M.p.: > 400 °C. ATR FTIR (podwer, cm⁻¹): ν 3448w, 3066vw, 2920vw, 2839vw, 1712vs, 1620 s, 1581vs, 1519 s, 1465 s, 1427w, 1408 m, 1357 m, 1288w, 1234 m, 1195 m, 1153w, 1103 s, 999 m, 960w, 894w, 829vs, 771 m, 748 m, 648w, 57w, 543 m, 513 m, 466w, 435w. Raman (cm⁻¹): 254w, 294vw, 352vw, 402vw, 429vw, 457vw, 500vw, 531w, 623vw, 723w, 755vw, 812vw, 838vw, 888vw, 992vw, 1040vw, 1076vw, 1090w, 1145 m, 1169 m, 1217 s, 1281 m, 1359 s, 1415 s, 1448 m, 1514w, 1572vs, 1723vw. Anal. Calcd. For C₂₆H₁₆CuN₂O₇: C, 58.70; H, 3.03; N, 5.27%. Found: C, 58.51; H, 2.80; N, 4.65. UV–Vis (0.011 mM; CHCl₃) λ_{\max} , nm (Log ϵ , M⁻¹ cm⁻¹): 349 (4.88), 435 (4.38).

8,8'-((1E,1'E)-(1,2-phenylenebis(azaneylylidene))bis(methaneylylidene))bis(7-hydroxy-2H-chromen-2-one)nickel(II) (4) Yield: 0.072 g (62%). M.p.: > 400 °C. ATR FTIR (podwer, cm⁻¹): ν 3537vw, 3074vw, 2954vw, 1728vs, 1620 s, 1581vs, 1523 s, 1489w, 1465 s, 1415 s, 1357 s, 1288w, 1253 m, 1266w, 1203 m, 1153w, 1103 s, 1006 s, 945w, 829vs, 771 s, 752vs, 648w, 590w, 574w, 555 s, 516 m, 466w, 443w, 416w. Raman (cm⁻¹): 265w, 305vw, 386vw, 436w, 471vw, 507vw, 548w, 631w, 725w, 740w, 760vw, 815vw, 845vw, 901vw, 1000w, 1041w, 1103 w, 1152 m, 1175w, 1220 m, 1235 m, 1281w, 1362 s, 1423 s, 1454 m, 1518w, 1575vs, 1727vw. Anal. Calcd. For C₂₆H₁₆N₂NiO₇: C, 59.24;

H, 3.06; N, 5.31%. Found: C, 59.05; H, 2.91; N, 4.87%. UV–Vis (0.025 mM; CHCl₃) λ_{\max} , nm (Log ϵ , M⁻¹ cm⁻¹): 366 (4.57), 483 (3.95).

8,8'-((1E,1'E)-((4,5-dimethoxy-1,2-phenylene)bis(azaneylylidene))bis(methaneylylidene))bis(7-hydroxy-2H-chromen-2-one)zinc(II) (5) Yield: 0.208 g (92%). M.p.: > 400 °C. ATR FTIR (podwer, cm⁻¹): ν 3437w, 3078w, 2939w, 2839w, 1732vs, 1712vs, 1616vs, 1585vs, 1512vs, 1481 s, 1408 s, 1373vs, 1265 s, 1126w, 1103w, 1010w, 918w, 837 s, 775w, 651w, 624w, 551w, 486w, 462w. Raman (cm⁻¹): 212 m, 343w, 400w, 716w, 773w, 1099 m, 1118 m, 1148 m, 1181 s, 1263 m, 1322 s, 1361vs, 1428 m, 1456w, 1481 m, 1515 m, 1569 s, 1585vs, 1619w. ¹H NMR (400 MHz, DMSO-*d*₆) δ 9.27 (s, 2H), 7.84 (d, *J*=8.9 Hz, 2H), 7.46 (d, *J*=8.5 Hz, 2H), 7.27 (s, 2H), 6.65 (d, *J*=8.5 Hz, 2H), 6.06 (d, *J*=8.9 Hz, 2H), 3.88 (s, 6H). ¹³C NMR (100 MHz, DMSO-*d*₆) δ 174.8, 160.3, 157.5, 152.7, 149.4, 145.3, 133.9, 132.7, 120.9, 107.3, 106.0, 99.3, 55.8. Anal. Calcd. For (C₂₈H₂₀N₂O₉Zn·2 H₂O): C, 53.39; H, 3.84; N, 4.45%. Found: C, 53.59; H 4.04; N, 4.59%. UV–Vis (0.018 mM; DMSO) λ_{\max} , nm (Log ϵ , M⁻¹ cm⁻¹): 364 (4.72), 4.39 (4.12), 451 (4.24), 260 (4.20).

8,8'-((1E,1'E)-((4,5-dimethoxy-1,2-phenylene)bis(azaneylylidene))bis(methaneylylidene))bis(7-hydroxy-2H-chromen-2-one)cobalt(II) (6) Yield: 0.119 g (71%). M.p.: > 400 °C. ATR FTIR (podwer, cm⁻¹): ν 3444 s, 3059w, 2939w, 2839w, 2360 s, 2337 s, 1732vs, 1716vs, 1616vs, 1581vs, 1519vs, 1462w, 1408 s, 1357 s, 1276 s, 12,46w, 1230w, 1199w, 1126w, 837 s, 374w. Raman (cm⁻¹): 287w, 393w, 443w, 509w, 536w, 635w, 660w, 680w, 731w, 783w, 1150w 1191 m, 1276 m, 1362 s, 1418 s, 1456 s, 1566vs. Anal. Calcd. For C₂₈H₂₀CoN₂O₉·0.5 H₂O: C, 56.39; H, 3.55; N, 4.70%. Found: C, 56.48; H 3.32; N, 5.08%. HRMS (ESI+) *m/z* Calcd. For [C₂₈H₁₈N₂O₈Co]⁺: 569.0395; found: 569.0387 [M]⁺. UV–Vis (0.015 mM; DMSO) λ_{\max} , nm (Log ϵ , M⁻¹ cm⁻¹): 361 (4.72), 257 (4.64), 475 (4.10).

8,8'-((1E,1'E)-((4,5-dimethoxy-1,2-phenylene)bis(azaneylylidene))bis(methaneylylidene))bis(7-hydroxy-2H-chromen-2-one)copper(II) (7) Yield: 0.148 g (88%). M.p.: > 400 °C. ATR FTIR (podwer, cm⁻¹): ν 3437 w, 3043w, 2935w, 2835w,

1724vs, 1604vs, 1581vs, 1516vs, 1465 s, 1404 s, 1377 s, 1361 s, 1273 s, 1246w, 1226w, 1192 s, 1153w, 1126w, 1103 s, 1014 s, 925w, 833 s, 775w, 729w, 651w, 624w, 586w, 528 s, 486w, 466w, 435w, 351vs. Raman (cm⁻¹): 254 m, 518 m, 773w, 851vw, 949 vw, 1115w, 1145w, 1182 m, 1264 s, 1354 s, 1415 s, 1455 m, 1508w, 1579 vs. Anal. Calcd. For (C₂₈H₂₀CuN₂O₉): C, 56.81; H, 3.41; N, 4.73%. Found: C, 56.81; H 3.23; N, 5.09%. HRMS (ESI+) *m/z* Calcd. For [C₂₈H₂₀N₂O₉Cu + C₃H₇NO]⁺: 664.0992; found: 663.4491 [M + C₃H₇NO]⁺. UV–Vis (0.045 mM; DMSO) λ_{\max} , nm (Log ϵ , M⁻¹ cm⁻¹): 360 (4.12), 420 (3.78), 266 (3.75).

8,8'-((1E,1'E)-((4,5-dimethoxy-1,2-phenylene)bis(azaneylylidene))bis(methaneylylidene))bis(7-hydroxy-2H-chromen-2-one)nickel(II) (8) Yield: 0.133 g (79%). Mp: > 400 °C. ATR FTIR (podwer, cm⁻¹): ν 3491w, 3062w, 2839w, 1735vs, 1712vs, 1616vs, 1604vs, 1585vs, 1519vs, 1465 s, 1411 s, 1361 s, 1276 s, 1249w, 1199 s, 1153w, 1126w, 1107 s, 1014 s, 937w, 833 s, 775w, 651w, 601w, 551w, 489w, 451w, 389w, 354w. Raman (cm⁻¹): 282w, 391w, 436vw, 503vw, 538 m, 593w, 629w, 726w, 778w, 858w, 930w, 1103w, 1117w, 1145w, 1187 m, 1270 s, 1342 s, 1357 s, 1421 s, 1453 s, 1524w, 1570vs. Anal. Calcd. For (C₂₈H₂₀N₂NiO₉): C, 57.28; H, 3.43; N, 4.77%. Found: C, 57.05; H 3.31; N, 4.91%. UV–Vis (0.055 mM; DMSO) λ_{\max} , nm (Log ϵ , M⁻¹ cm⁻¹): 367 (4.25), 267 (3.88), 465 (3.67).

Synthesis of 8,8'-((1E,1'E)-((4,5-dimethoxy-1,2-phenylene)bis(azaneylylidene))bis(methaneylylidene))bis(7-hydroxy-2H-chromen-2-one)platinum(II) (9)

Sodium acetate (0.032 g, 0.40 mmol) was added to a stirred solution of L₂ (0.100 g, 0.020 mmol) in DCM (20 mL) and DMSO (1 mL). The reaction mixture was refluxed for 30 min. A solution of K₂PtCl₄ (0.081 g, 0.020 mmol) in DMSO (1 mL) was then added. The reaction mixture was refluxed again for 16 h. After that, DCM was removed under vacuum and the resulting crude solid was purified by centrifugation. The solid was washed with DMSO (2 × 10 mL), ethyl acetate (6 × 10 mL), acetone (1 × 10 mL) and diethyl ether (2 × 10 mL), respectively. **9** was obtained as a red solid. Yield: 0.098 g (71%). M. p.: 297 °C (decomposition). ATR FTIR (podwer,

cm^{-1}): ν 3059vw, 2947vw, 2835vw, 1708vs, 1612vs, 1577vs, 1512vs, 1462 s, 1408 s, 1354 s, 1276 s, 1230 s, 1188 s, 1153w, 1111 s, 1087w, 1037w, 1010 s, 941w, 921w, 829vs, 771 s, 605w 555 s, 470 s, 443w. Raman (cm^{-1}): 125 s, 242w, 441w, 512w, 639w, 768w, 1111 m, 1126 m, 1149 m, 1187 m, 1277 s, 1335 s, 1368 s, 1423 s, 1465w, 1513w, 1580vs. Anal. Calcd. For ($\text{C}_{28}\text{H}_{18}\text{N}_2\text{O}_8\text{Pt}$): C, 47.67; H, 2.57; N, 3.97%. Found: C, 47.66; H, 2.83; N, 3.57%. UV–Vis (0.045 mM; DMF) λ_{max} , nm (Log ϵ , $\text{M}^{-1} \text{cm}^{-1}$): 370 (4.24), 266 (3.80), 473 (3.57), 506 (3.50).

X-ray structure determination of 5 and 6

Recrystallization of compounds **5** and **6** was carried out via slow evaporation of mixtures of DMSO:DMF (1:1) and THF:DMSO:DMF:EtOH (1:1:1:1), respectively. These procedures afforded crystals of suitable size and quality for single-crystal X-ray diffraction. The collected data and refinement details are summarized in Table S1. In the refinements, all the non-hydrogen atoms were anisotropically treated, and the hydrogen atoms were generated geometrically, placed in the calculated positions ($\text{C}-\text{H}=0.93$ – 0.96 Å) and included as riding contributions with isotropic displacement parameters set at 1.2–1.5 times the U_{eq} value of the parent atom. The H atoms belonging to water molecules in the coordination sphere of the Co and Zn atoms were located in different density maps and refined with suitable geometric constraints. The crystal structures were refined using the SHELXL2014 program (Sheldrick 2015). The graphic material was prepared using Mercury 3.10.3 software (Macrae et al. 2008).

Theoretical calculations

DFT calculations

Density Functional Theory (DFT) computations were performed with the Gaussian16 series of programs (Frisch et al. 2016). The M06 functional proposed by Truhlar and Zhao (Zhao and Truhlar 2004, 2005, 2008; Zhao et al. 2005) was used in all computations. This functional can provide a reliable description of transition metals and medium-range π – π interactions at the same time (Bottoni et al. 2013; Giacinto et al. 2014, 2015). The 6-31G* basis

set, included in the Gaussian package, was used for all atoms except the metal atoms, which were described with the energy-adjusted pseudo-potential basis set proposed by Preuss and co-workers (denoted as sdd pseudo-potentials in the Gaussian 16 formalism) (Andrae et al. 1990). The multiplicity was singlet for systems including Ni, Pt and Zn, quartet with Co and doublet with Cu.

MD calculations

We started from a crystal structure of a G4 helix in complex with a salphen ligand analogous to those examined here [PDB code 3QSC (Campbell et al. 2012)]. The DNA helix was parametrized with the parmBSC0 force field (Pérez et al. 2007) adding the parmBSC1 corrections (Ivani et al. 2015). The partial charges of the atoms of the ligands were derived from quantum mechanical calculations by means of the RESP approach (Bayly et al. 1993; Wang et al. 2000) at the HF/6-31G* level of theory. The bonded parameters and the Lennard–Jones coefficients were taken from the GAFF force field (Wang et al. 2004). For the coordination complexes, the bonded parameters involving the central metal ions were calculated with the methodology presented by Seminario for metals in biological environments (Seminario 1996; Carvalho et al. 2013). The DNA helix was simulated in presence of the organic ligands at their doubly anionic state (\mathbf{L}_1 and \mathbf{L}_2), but also in their neutral, protonated form (\mathbf{HL}_1 and \mathbf{HL}_2), and as coordination complexes (\mathbf{ML}_1 and \mathbf{ML}_2). Finally, the apo-form of the DNA quadruplex (APO) was also simulated for comparison adding to seven MD runs in total. It is important to note, that molecular mechanics-based methods do not account explicitly for the electronic features of transition metals. Thus, this technique can be better used to compare different chemical states of the ligands, as those described above, rather than various complexes differing only on the coordinated metal.

For the MD calculations, we first defined a simulation box by imposing a minimum distance of 1.4 nm to the DNA–ligand complex, and we filled it with TIP3P (Jorgensen et al. 1983) water molecules. Sodium ions were incorporated to the solution to reach the electroneutrality of the system, and additional sodium chloride was used to reach an ionic strength of 150 mM to reminisce physiological

conditions. Then, the solvent was allowed to relax by performing a minimization with the steepest-descent method. The system proceeded to be heated for 500 ps with the V-rescale thermostat ($\tau_T=0.1$ ps) in the NVT ensemble until 310 K. We then pressurized the system to 1 bar with a 500 ps-long simulation in the NPT ensemble with the isotropic Parrinello-Rahman barostat (Parrinello and Rahman 1981) ($\tau_P=2.0$ ps and $\kappa=4.5 \times 10^{-4}$ bar $^{-1}$). All the production runs lasted 200 ns, discarding the first 25 ns as equilibration. Furthermore, all bonds were constrained with the LINCS algorithm (Hess et al. 1997) allowing using a timestep of 2 fs. Short-range non-bonded interactions were explicitly calculated within a radius of 1.2 nm of each atom, whereas long-range electrostatic interactions were accounted for with the PME method (Darden et al. 1993) of fourth order. All the MD runs were carried out with Gromacs v2019.2. The trajectories' analysis was performed with the MDAnalysis python library.

Cytotoxicity Activity

Cytotoxicity activity was measured by a colorimetric method with MTT. In this procedure, carcinoma HeLa cells and noncancerous HaCaT and HFF-1 cells were exposed to different concentrations (10, 30, 40, 50, 70, and 100 μ M) of each of the evaluated ligands (**L**₁ and **L**₂) and complexes (**1**–**9**). Briefly, 96-well flat-bottomed plates, 2×10^5 cells/mL were grown with four replicate wells for each treatment. After 24 h, the medium was removed from each well and the cells were treated. A stock solution (20 mM in DMSO) of each of the compounds was prepared to ensure a maximum DMSO concentration of 0.5% in the administered dilutions (each dilution was made using DMEM supplemented with 1% of penicillin/streptomycin). At this concentration the solvent had no significant toxic effects on the cell lines used. A negative control (cells exposed to DMEM with 0.5% DMSO), and a blank of the negative control and dilutions (wells without cells but with the corresponding solution) were included in each experiment. The microplates were incubated for 48 h at 37 °C and 5% CO₂ in a humidified incubator. After incubation, 10 μ L of MTT (5 mg/mL) was added to each well, and the cells were incubated for an additional 2 h. Then, the medium was removed and 100 μ L of DMSO per well was added to dissolve the formazan crystals. The

absorbance was measured at 595 nm (using a reference wavelength of 655 nm) in a microplate reader. The results were expressed as the percentage of living cells as calculated from MTT reduction, assuming the absorbance of the control cells as 100%. The IC₅₀ values of the evaluated compounds were obtained from the dose–response curve of percent viability versus test concentrations.

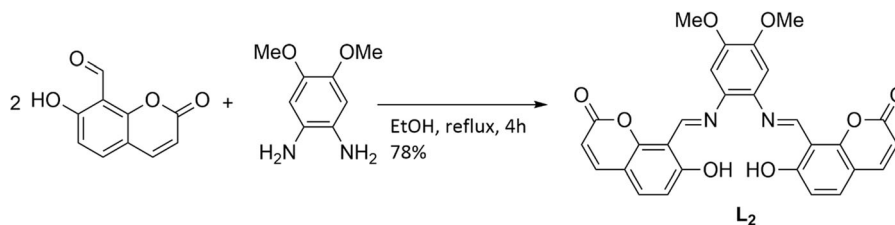
Results and discussion

Synthesis and characterization of **L**₂

L₂ was synthesized by the double condensation reaction between 8-formyl-7-hydroxycoumarin and 1,2-dimethoxy-4,5-dinitrobenzene in EtOH under reflux (Scheme 1) and was isolated by simple purification as an orange solid in high yield.

L₂ was characterized by elemental analysis, high-resolution mass spectrometry (HRMS) and UV–Vis, fluorescence, FTIR, Raman ¹H and ¹³C NMR spectroscopy (Fig. S1–S8). The ¹H and ¹³C NMR chemical shifts were assigned with the aid of DEPT 135 and HSQC experiments. The ¹H NMR spectrum showed a singlet at 14.88 ppm corresponding to the protons of the phenolic group (–OH). This downshift is probably due to an intramolecular hydrogen bond between this moiety and the nitrogen atom of the imine (OH⋯N=C–) (Nuñez-Dallos et al. 2016). The singlet at 9.33 ppm is assigned to the protons of azomethine groups (–N=C–H). The coupled doublets at 7.65 ($J=9.5$ Hz) and 6.26 ($J=9.5$ Hz), were assigned to the vinylic protons of the coumarin moiety and the coupled doublets at δ 7.44 ($J=8.8$ Hz) and 6.95 ($J=8.8$ Hz) were assigned to the protons on the aromatic structure. This assignment was confirmed by the integrals of the peaks. Additionally, the HRMS (ESI+) spectrum recorded in acetonitrile, showed the molecular ion peak which is consistent with the molecular weight of [**L**₂+H]⁺.

The solid-state FTIR spectrum (Fig. S1) showed a broad band between 3591 and 3460 cm^{–1} assigned to ν (O–H) of the phenolic group (O–H) (Kilic et al. 2018). This broad band also indicates the formation of an intramolecular hydrogen bond (OH⋯N=C–) (Sharma et al. 2016). The weak bands between 3062 and 2839 cm^{–1} correspond to the ν (C–H) of the methoxy group (–OCH₃) and the unsaturated carbons.



Scheme 1 Synthesis of **L₂**

The band assigned to $\nu(\text{C}=\text{O})$ was observed as two contiguous bands at 1743 and 1716 cm^{-1} . This result is explained by the Fermi resonance which is characteristic of compounds featuring unsaturated lactones in their structure (Jones et al. 1959; Winston and Kemper 1971). The $\nu(\text{C}=\text{N})$ band is observed at 1612 cm^{-1} , and the shoulder of this band at a shorter wavenumber is attributed to the $\nu(\text{C}=\text{C})$ stretching vibration (Larkin 2018a).

The absorption electronic spectrum of **L₂** was acquired in DMSO (Fig. S8). The band with the highest molar absorptivity was observed at 371 nm and was attributed to the π - π^* electronic transitions of the conjugated system of the ligand (Sharma et al. 2016; Nuñez-Dallos et al. 2017). A shoulder band, observed at 412 nm, was assigned to the π - π^* electronic transition of the imine moiety ($\text{C}=\text{N}$) (Kajal et al. 2013). The shoulder in 449 nm was attributed to the n - π^* electronic transition due to the promotion of an electron from the unpaired electrons of the nitrogen atom to an antibonding π orbital of the azomethine group (Aranha et al. 2007).

Synthesis and characterization of 2–9

The synthesis of complex **1** (using **L₁**) has been previously reported by our group (Scheme 2) (Nuñez-Dallos et al. 2016, 2017). On this basis, the syntheses of **2–9** were also carried out by the deprotonation of the hydroxyl group of the ligand (**L₁** or **L₂**) by the action of the acetate salt (Schemes 2, 3). The syntheses of all complexes are favored by the chelate effect (ONNO) and the Zn(II), Co(II), Cu(II) and Ni(II) complexes (**2–8**) are also favored by the Pearson acid–base concept as these metals are intermediate acids. In contrast, the synthesis of Pt(II) complex **9**, bearing a soft acid, is less favored (Schweitzer and Pesterfield 2010), which is evident in its prolonged reaction time.

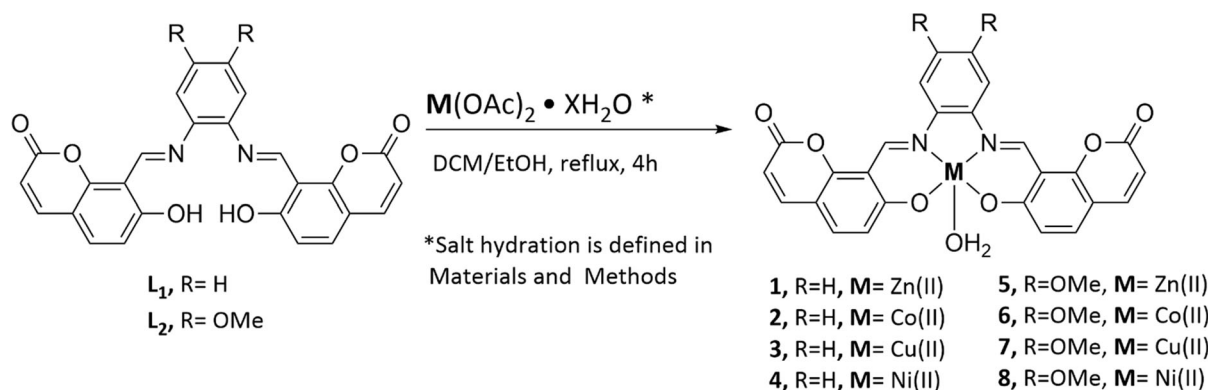
All complexes presented a 1:1 ligand-to-metal ratio as indicated by elemental analysis. This technique also led us to propose the presence of crystallization or coordination water molecules, which was corroborated using TGA. Further characterization of the complexes was carried out by HRMS, X-ray crystallography and Raman, FTIR, UV–Vis, fluorescence and NMR spectroscopy (Fig. S9–S46) and is described in the following sections.

NMR spectroscopy

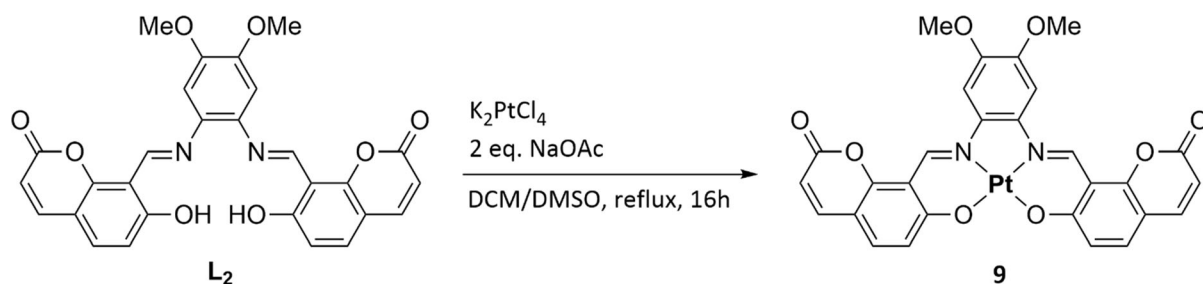
Among all the synthesized complexes, **4**, **5**, **8** and **9** are diamagnetic. Nevertheless, due to their poor solubility in common deuterated solvents, only **5** was characterized by NMR (Fig. S42–S44). The coordination of the metallic center entails the deprotonation of the ligand, hence, the ^1H NMR spectrum in $\text{DMSO-}d_6$ of **5** is characterized by the lack of the phenolic proton of **L₂** at 14.88 ppm in CDCl_3 . The absence of this proton is also evident in the reported spectrum of **1** (Nuñez-Dallos et al. 2017). The distinctive signals of **L₂** are also present in the spectrum of **5**. Nevertheless, as the spectra of **5** and **L₂** were acquired in different deuterated solvents, the effect of the coordination of the Zn(II) metallic center on the shift in the signals is not possible to determine.

Infrared and Raman spectroscopy

The FTIR spectra of the complexes were compared to the spectra of the corresponding ligand (Fig. S1 or S17), and the most important bands are listed in Table 1. In general, the spectra of the complexes presented a shift to higher or lower wavenumbers which indicates a change in the rigidity of the chemical bonds of the ligand with respect to the



Scheme 2 General reaction for the synthesis of complexes **1–8** (**M**=Co(II), Cu(II), Ni (II), and Zn(II))



Scheme 3 Synthesis of complex **9**

Table 1 Characteristic bands in the FTIR and Raman spectra of ligands and complexes

Compound	FTIR (cm^{-1})						Raman (cm^{-1})	
	$\nu(O-H)_{Ph}^a/H_2O$	$\nu(C-H)$	$\nu(C=O)$	$\nu(C=N)$	$\nu(C=C)$	$\nu(C-O)_{Ph}^a$	$\nu(M-O)$	$\nu(M-N)$
L ₁	3421	3070	1732	1612	1589	1099	–	–
2	3560	3094–2839	1728	1620	1578	1103	434	538
3	3449	3067–2839	1712	1620	1581	1103	254	531
4	3537	3074–2954	1728	1620	1581	1103	265	436
L ₂	3591–3460	3062–2832	1743–1716	1612	– ^b	1122	–	–
5	3437	3078–2839	1732–1712	1616	1585	1126	343	400
6	3444	3059–2839	1732–1716	1616	1581	1126	443	536
7	3447	3043–2835	1724	1604	1581	1126	254	518
8	3491	3062–2839	1735–1712	1616	1585	1126	282	436
9	–	3059–2835	1708	1612	1577	1126	441	512

^a *Ph* Phenolic

^b Overlapped with the $\nu(C=N)$ band

coordination with the metal center (Castillo et al. 2016).

As the deprotonation of the phenolic group of the ligands was necessary for the formation of complexes

2–9, the band assigned to the $\nu(O-H)$ phenolic of **L**₁ and **L**₂ was not observed in the complexes. Instead, the broad band observed between 3437 and 3560 cm^{-1} for complexes **2–8** corresponds to the

O–H stretching vibration of lattice and coordinated water molecules. The presence or lack (for complex **9**) of this band corroborates the results indicated by elemental analysis and TGA. The $\nu(\text{C-H})$ stretching band is present in the spectra of all complexes between 3094 and 2835 cm^{-1} . Compared to corresponding band in the spectrum of L_2 , the $\nu(\text{C=C})$ stretching band appears as a well-defined band for **5–9** in a range between 1577 and 1585 cm^{-1} .

Additionally, the $\nu(\text{C=O})$ stretching band observed for **2–4** is in the range between 1712 and 1728 cm^{-1} . The two contiguous bands assigned to $\nu(\text{C=O})$ stretching in the spectrum of L_2 , are also observed in the spectra of complexes **5** (1732 and 1712 cm^{-1}), **6** (1732 and 1716 cm^{-1}) and **8** (1735 and 1712 cm^{-1}). Whereas, $\nu(\text{C=O})$ stretching is observed as a band with a shoulder in the spectra of complexes **7** (1724 cm^{-1}) and **9** (1708 cm^{-1}). The variation of the shape of the $\nu(\text{C=O})$ band according to the complex, can be attributed to a mild modification in the Fermi resonance caused by the different metallic centers.

The ligands coordinate to the metal ions through the imine nitrogen and the phenolic (ph) oxygen as evidenced by the shift of the $\nu(\text{C=N})$ and $\nu(\text{C-O})_{\text{ph}}$ stretching bands. For complexes **2–4** these bands shift to a greater wavenumber compared to L_1 . The corresponding band of $\nu(\text{C=N})$ stretching in the spectra of **5–9** is found between 1604 and 1616 cm^{-1} . It is observed to be shifted 4–8 cm^{-1} to a higher or lower wavenumber with respect to the $\nu(\text{C=N})$ stretching band at 1612 cm^{-1} for L_2 . The band corresponding to $\nu(\text{C-O})_{\text{ph}}$ of L_2 (1122 cm^{-1}) is observed to be shifted to a higher wavenumber in the spectra of **5–9**. Additionally, compared to the respective free ligand, there is a decrease in the intensity of the $\nu(\text{C=N})$ and $\nu(\text{C-O})_{\text{ph}}$ bands with respect to that of other characteristic bands in the spectra of all complexes. This decrease could be due to the reduction in the electronic density of the donor atoms (ONNO), which result in a greater bond vibration and a decrease in the change in the dipole moment of the bonds (Kavitha and Anantha Lakshmi 2017; Larkin 2018b). Furthermore, the shift to a greater wavenumber could be related to the reduction in the electronic density on the coordinating atom, which results in an increase of the vibrational frequency (Kavitha and Anantha Lakshmi 2017; Larkin 2018b).

Raman spectroscopy was used to corroborate the coordination of the ligands through the oxygen and nitrogen atoms to the metals, as it was possible to assign the $\nu(\text{M-O})$ and $\nu(\text{M-N})$ stretching modes. The respective assignments for all the complexes **2–9** are shown in Table 1. For complex **5**, $\nu(\text{Zn-O})$ and $\nu(\text{Zn-N})$ are observed at 343 and 404 cm^{-1} , respectively. For **2** and **6**, the bands between 434 and 538 cm^{-1} where assigned to $\nu(\text{Co-O})$ and $\nu(\text{Co-N})$. The spectra of complexes **3** and **7** showed the $\nu(\text{Cu-O})$ and $\nu(\text{Cu-N})$ bands in the range between 254 and 531 cm^{-1} . The $\nu(\text{Ni-O})$ and $\nu(\text{Ni-N})$ stretching modes of complexes **4** and **8** were observed in the range between 265 and 436 cm^{-1} . For **9**, the bands attributed to $\nu(\text{Pt-O})$ and $\nu(\text{Pt-N})$ were observed in 441 and 512 cm^{-1} , respectively (Socrates 2004; Nakamoto 2008; Suffren et al. 2012; Datta et al. 2018).

Thermal analysis

A thermogravimetric analysis was performed to verify the presence of crystallization and coordination water molecules in the proposed molecular formula of all complexes. All the mass loss assignments were proposed, as detection was not possible. All complexes presented a step by step decomposition as it was indicated by the temperature of the DTG (TGA curve derivative) (Fig. S9–S16). Complexes **2**, **3**, **4**, **7** and **8** presented a mass loss of 3.41, 3.38, 3.41, 3.04 and 3.07% (calcd. 3.26, 3.53, 3.01, 3.01 and 2.81%), respectively, in the temperature range from 215 to 400 °C corresponding to the loss of a coordinated water molecule. Complex **5** showed a mass loss of 5.72% (calcd. 4.39%) at 194 °C attributed to the loss of two water molecules of hydration and a two-step mass loss of 30.39% (calcd. 31.22%) at 400 and 537 °C, which may correspond to the loss of a coordination water molecule and a coumarin fragment $\text{C}_{10}\text{H}_5\text{O}_3$, respectively. **6** also presented a two-step loss of 4.02% (calcd. 3.97%) at 36 and 215 °C corresponding to the loss of half of a crystallization water molecule and a coordination water per complex unit. According to TGA results, Pt (II) complex **9** did not present any coordinated water molecules. Regarding the stability, the total mass loss of all complexes oscillated from 26.30% to 68.19%. **9** showed the lowest mass loss (26.3%), whence, the metallic residue remaining above 700 °C

corresponded to the highest percentage. In spite of that, **2–8** presented higher thermal stability as their first organic loss occurred at higher temperatures (from 428 °C to 537 °C) than Pt(II) complex **9** (299 °C).

Absorption electronic properties

The UV–Vis spectra of **L₁**, **L₂** and complexes **2–9** were obtained in the range from 290 to 800 nm at concentrations from 1.1×10^{-5} to 5.5×10^{-5} M, using CHCl_3 , DMF and DMSO as solvents. The assignments of the bands in the UV–Vis spectra of the ligands and complexes are presented in Table 2.

The UV–Vis spectra of **2–4** were acquired in CHCl_3 and presented bands attributed to intra-ligand electronic transitions present in **L₁** and additional intra-ligand bands could also be observed in the spectra of some complexes (Fig. 2a). The band associated with the $\pi-\pi^*$ electronic transitions of the C=C chromophore was observed between 349 and 366 nm for these complexes (Houjou et al. 2017). This band for **2–4** undergoes a bathochromic shift of 22 to 39 nm with respect to the band of **L₁**. Complex **2** presented an additional intra-ligand band at 412 nm, attributed to the $\pi-\pi^*$ electronic transition of the

azomethine moiety (C=N) (Fig. 2a) (Akbari and Alinia 2013).

The band assigned to the $n-\pi^*$ transition of the unpaired electrons of the $-\text{C}=\text{N}$: chromophore to an antibonding π orbital of the double bond was observed in the range between 435 and 468 nm for **1–4** (Akbari and Alinia 2013). The location of this band indicates a hypsochromic shift with respect to that of **L₁**. This shift corresponds to the most remarkable change in the spectra of the complexes, as the availability of the unpaired electrons of the imine group (C=N:) is compromised by the coordination of **L₁** to each metallic center (Aranha et al. 2007; Kavitha and Anantha Lakshmi 2017; Nuñez-Dallos et al. 2017). The low absorptivity bands at 535 and 578 nm that are observed in the spectrum of complex **2** might be assignable to d-d transitions for square pyramidal geometry (Borthakur et al. 2015).

The spectra of **5–8** were obtained in DMSO, while the spectrum of **9** was obtained in DMF. The analysis of the spectra of the complexes was performed by comparing the observed bands of **L₂** in DMSO or DMF as appropriate. The spectra of **5–9** showed bands assignable to the intraligand electronic transitions of **L₂**. A band attributed to the $\pi-\pi^*$ (C=C) electronic transition is observed between 360 and

Table 2 UV–Visible band assignment for ligands and complexes

Compound (Concentration/M)	Solvent	Band assignment λ (log ϵ)/nm ($\text{M}^{-1} \text{cm}^{-1}$)			
		$\pi-\pi^*$ (C=C) ^[a]	$\pi-\pi^*$ (C=N)	$n-\pi^*$ (C=N)	<i>d-d</i>
L₁ (2.5×10^{-5})	CHCl_3	327 (4.63)	–	470 (3.33)	–
2 (1.7×10^{-5})	CHCl_3	350 (4.69)	412 (4.32) ^b	446 (4.20) ^b	535 (3.71) ^b , 578 (3.39) ^b
3 (1.1×10^{-5})	CHCl_3	349 (4.88)	–	435 (4.38)	–
4 (2.5×10^{-5})	CHCl_3	366 (4.57)	–	468 (3.97)	–
L₂ (1.5×10^{-5}) (2.4×10^{-5})	DMSO	371 (4.65)	412 (4.54) ^b	449 (4.38) ^b	–
	DMF	373 (4.45)	412 (4.34) ^b	442 (4.26) ^b	–
5 (1.8×10^{-5})	DMSO	364 (4.47)	412 (4.14)	451 (3.99)	–
6 (1.5×10^{-5})	DMSO	361 (4.72)	412 (4.33) ^b	475 (4.10)	–
7 (4.5×10^{-5})	DMSO	360 (4.12)	420 (3.78)	484 (3.56)	–
8 (5.5×10^{-5})	DMSO	367 (4.25)	– ^c	465 (3.67)	–
9 (4.5×10^{-5})	DMF	370 (4.24)	– ^c	473 (357)	(3.50)

^a Maximum absorbance of all compounds

^b Shoulder (log ϵ value calculated for the given wavelength)

^c Shoulder between 395 and 412 nm

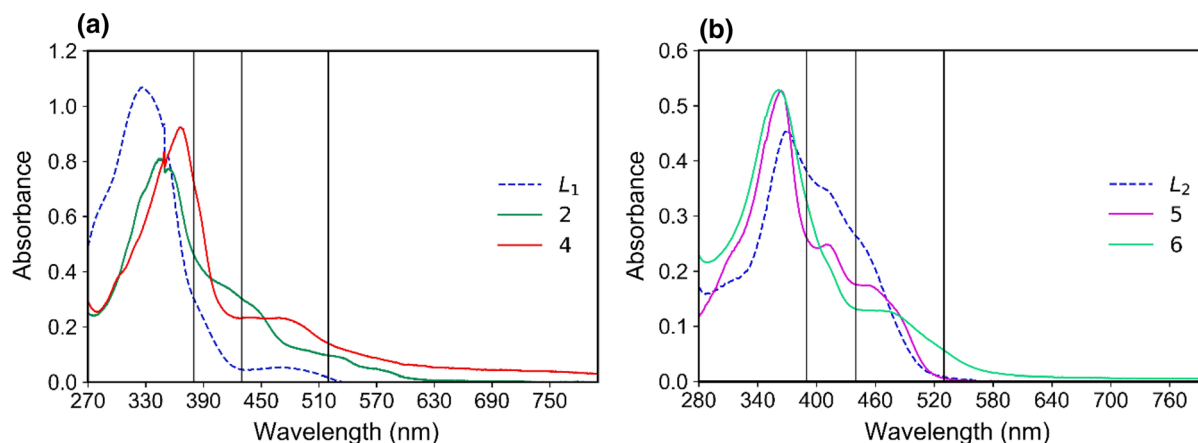


Fig. 2 Absorption electronic spectra of **a** L_1 and the complexes **2** and **4**, and **b** L_2 and the complexes **5** and **6**. (Color figure online)

370 nm for **5–9** (Nuñez-Dallos et al. 2016; Sharma et al. 2016). Compared to the corresponding band in the spectrum of L_2 (371 nm or 373 nm in DMSO or DMF, respectively), this band is shifted to a shorter wavelength. The π - π^* transition of the azomethine moiety (C=N) appears as a well-defined band for **5** and **7** at 412 and 420 nm, respectively (e.g. Figure 2b). This transition was observed as a mild shoulder at a wavelength between 395 and 412 nm in the spectra of **6**, **8** and **9** (e.g. Fig. 2b). The change in the molar absorptivity of this band (π - π^* ; C=N) with respect to the observed bands in L_2 and the other transitions observed for **6**, **8** and **9**, might be an indication of the coordination between the nitrogen atom of the imine and the metal center (Table 2). The band attributed to the n - π^* electronic transition of the unpaired electrons of the imine was observed in a range between 451 and 484 nm for **5–9**. This band presented a bathochromic shift with respect to the band in the spectrum of L_2 (449 or 442 nm in DMSO or DMF, respectively). This shift coincides with the most notable change and is also related to the coordination of the unpaired electrons of the imine (Aranha et al. 2007; Kavitha and Anantha Lakshmi 2017; Nuñez-Dallos et al. 2017). The spectrum of **9** showed a shoulder at 506 nm, probably due to d - d transitions of square-planar complexes (Borthakur et al. 2015).

Emission electronic properties

The effect of coordination on the emission electronic properties of L_1 and L_2 was investigated at room

temperature. The excitation wavelength selected to acquire the spectra was the wavelength of maximum absorbance of each compound (Table 2). The fluorescence spectra of L_1 and complex **1** are presented in Fig. 3a. The spectra of complexes **2–4** are not shown, as they did not exhibit any appreciable emission bands under these conditions. L_1 presented a strong emission band at 554 nm probably due to the π - π^* transition of the conjugated system. Clearly, **1** presented the strongest emission (at 542 nm) among complexes **1–4**. The emission spectra of L_2 and complexes **5–9** are shown in Fig. 3b. Compared to L_2 , which exhibited a less intense band at 479 nm, complex **5** presented an enhanced emission intensity at 492 nm. Complex **6** presented an emission band with a similar intensity at 459 nm. Additionally, the coordination to the Cu(II), Ni(II) and Pt(II) metal centers resulted in quenching of the fluorescence of L_2 as observed for **7–9**.

The fact that Zn(II) complexes **1** and **5** showed high or enhanced emission compared to that of the respective ligand can be attributed to the d^{10} nature of the metal. The complete filling of d orbitals prevents metal-centered electronic transitions that can result in nonradiative decay of the excited state (Balzani et al. 2007). Furthermore, it is well known that d^{10} metal ions can yield highly emissive materials (Allendorf et al. 2009). As the Zn(II) core is difficult to oxidize or reduce due to its electronic configuration, the emission bands are not attributed to metal-to-ligand charge transfer (MLCT) or ligand-to-metal transfer (LMCT) (Xie et al. 2008). Alternatively, they can be assigned to intraligand π - π^* electronic emission

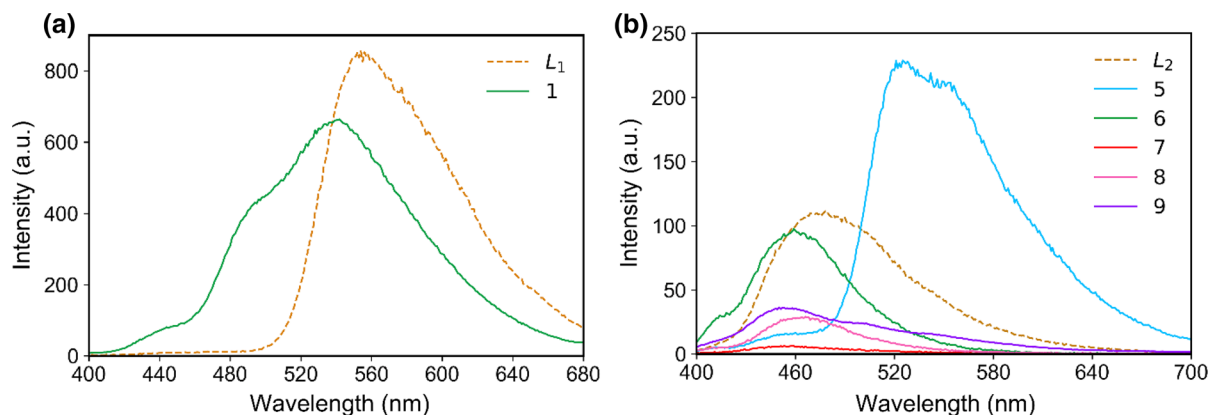


Fig. 3 Emission spectra of **a** L_1 ($\lambda_{em}=554$ nm, 2.5×10^{-5} M in $CHCl_3$) and **1** ($\lambda_{em}=542$ nm; 3.3×10^{-5} M in $CHCl_3$); and **b** L_2 ($\lambda_{em}=479$ nm, 1.5×10^{-5} M in DMSO) and the complexes **5** ($\lambda_{em}=492$ nm, 1.8×10^{-5} M in DMSO), **6** ($\lambda_{em}=459$ nm, $1.5 \times$

10^{-5} M in DMSO), **7** ($\lambda_{em}=459$ nm, 4.5×10^{-5} M in DMSO), **8** ($\lambda_{em}=466$ nm, 5.5×10^{-5} M in DMSO) and **9** ($\lambda_{em}=450$ nm, 3.3×10^{-5} M in DMF). (Color figure online)

(Xie et al. 2008). It is noticeable that complexes **2–4** and **7–9** quench the inherent fluorescence of the ligand (Dogahneh et al. 2016) upon coordination. This quenching occurs because the emission from paramagnetic transition metal complexes or diamagnetic metal complexes with partially filled d orbitals is generally not strong, as $d-d$ transitions can lead to competitive non-radiative decay of the mixed fluorophore/metal $\pi-\pi^*/d-d$ state and the fluorophore-localized $\pi-\pi^*$ state (Allendorf et al. 2009; Yang et al. 2015). In spite of the latter, the coordination of the paramagnetic Co(II) metal ion to L_2 did not result in a complete quenching of the fluorescence of the ligand in complex **6** (Fig. 3b) as has also been reported for similar Co(II) complexes (Dogahneh et al. 2016).

Description of crystal structures

With the objective of making the characterization of the complexes more meaningful and to be able to suggest a possible mechanism of biological action an X-ray diffraction study was undertaken. Crystals obtained from the complexation reactions of the coumarin salphen ligand (L_2) with Zn(II) and Co(II) ions were investigated by X-ray diffraction crystallography (the data are summarized in Table S1). Unfortunately, all attempts to obtain single crystals from the other complexes for X-ray studies were unsuccessful. The reactions afford molecules characterized by marked planarity, as shown in Fig. 4.

Crystal structures of **5** and **6** are isostructural, with a monoclinic $P2_1/n$ space group type and unit cell dimensions that differ in less than 0.06 \AA in a , b and c , and 0.05° in β .

In each complex, the coumarin groups have dihedral angles between their least-squares mean planes of $4.37(8)^\circ$ and $3.75(8)^\circ$ for **5** and **6**, respectively. Additionally, the dihedral angles between the 1,2-dimethoxybenzene moieties and the coumarin groups are $4.56(8)^\circ/4.60(7)^\circ$ and $4.62(7)^\circ/4.22(7)^\circ$, in compounds **5** and **6**, respectively, endowing the molecules with a high level of planarity. Only one water molecule is out of this planar conformation, forming an axial configuration in the coordination sphere of Zn(II) and Co(II) in each complex. Both metallic atoms present the same five-coordinate geometry, in which each is bonded to the salphen type ligand and one water molecule. Analysis using the τ descriptor for the five-coordinate centers gives a value of 0.05 for both complexes, suggesting a stereochemistry more matched to a square-pyramidal (SP) geometry (extreme forms: $\tau=0.00$ for SP and $\tau=1.00$ for trigonal-bipyramidal) (Addison et al. 1984). The calculated polyhedral volumes are 6.447 \AA^3 and 6.484 \AA^3 for **5** and **6**, respectively. The planarity observed in the conformation of the coumarin groups allows the formation of the intramolecular C1(A, B)–H1(A, B)–O2(A, B) hydrogen bonds (H–O length of 2.32 \AA).

Intermolecular C8(A, B)–H8(A, B)–O3(B, A) hydrogen bonds join molecules along the [001]

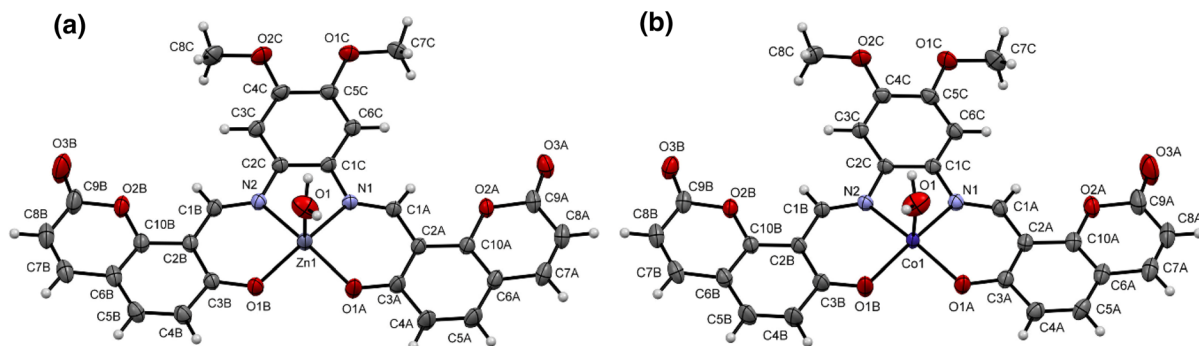


Fig. 4 The molecular structures of **a 5** and **b 6**, showing anisotropic displacement ellipsoids at the 30% probability level. (Color figure online)

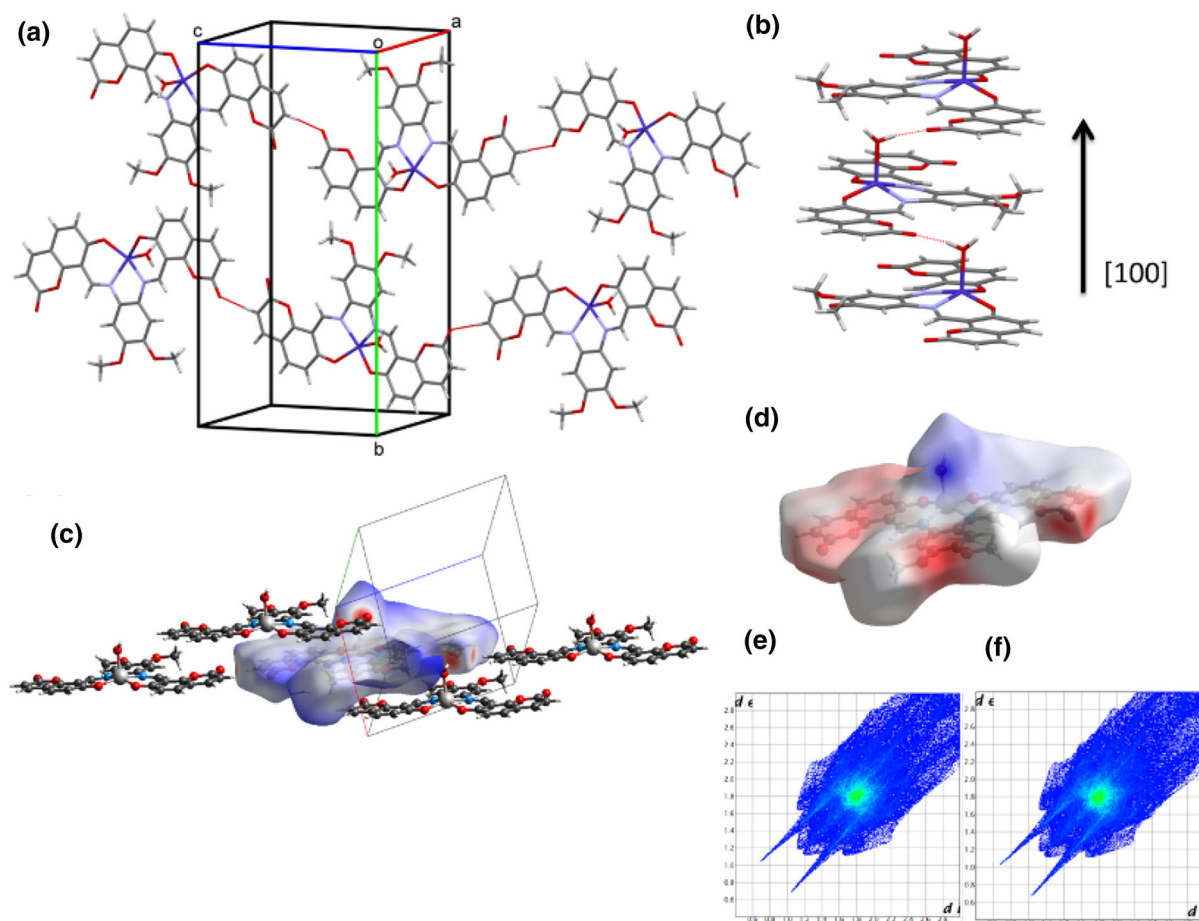


Fig. 5 Crystal structure representing the C–H–O hydrogen-bonds interactions for **5** and **6** along **a** [001] and **b** [100]. **c** A view of the Hirshfeld surface mapped over d_{norm} , emphasizing the intermolecular interactions H–O/O–H. **d** The electrostatic

direction through the coumarin groups (symmetry codes: $-1/2+x, 3/2-y, -3/2+z$ and $-1/2+x, 1/2-y, -$

potential with positive and negative potential indicated in blue and red, respectively. **e** and **f** full 2D-fingerprint plots for **5** and **6**, respectively. (Color figure online)

$3/2+z$; H–O lengths of 2.30 Å and 2.29 Å, for **5** and **6**, respectively). Figure 5a shows the molecular

chains. In addition to these interactions, strong intermolecular O1–H1···O3(B, A) hydrogen bonds join parallel molecular chains along the [100] direction involving the water molecules (symmetry codes: $1/2+x, 3/2-y, -1/2+z$ and $-1/2+x, 1/2-z, -1/2+z$; H–O lengths of 1.88(3) Å and 1.84(3) Å, for **5** and **6**, respectively) forming (010) sheets joined along the [010] direction through dispersion and other van der Waals forces (Fig. 5b). The supramolecular architecture is assisted by C7C–H7CA–Cg_{1,2} interactions (Cg₁ and Cg₂ are the centroids of the C2B/C10B and C2A/C10A rings for **5** and **6**, respectively) with H– π distances of 2.95 Å and 2.94 Å for the Zn and Co complexes, respectively. The arrangement of the molecules allows the formation of important π – π stacking interactions involving distances of ~3.5–3.8 Å between the centroids of the aromatic rings.

The intermolecular interactions were confirmed using *CrystalExplorer 3.1* software (Wolff et al. 2012). Generating Hirshfeld surfaces, mapped over d_{norm} (analysis of the contact distances d_i and d_e from the HF surface to the nearest atom inside and outside, respectively). The electrostatic potential was calculated using TONTO, a Fortran-oriented system for quantum chemistry and crystallography (TONTO is available at hirshfeldsurface.net), and subsequently mapped over the HF surface using the STO-3G basis set at the Hartree–Fock level of theory over the range of ± 0.14 a.u. (Jayatilaka et al. 2005; Spackman et al. 2008). In Fig. 5c, the intermolecular interactions are observed as bright-red spots over d_{norm} . C–H···O interactions are the most important in the construction of the crystal with H–O/O–H contacts constituting 23.0 and 22.9% of the total HF surface for **5** and **6**, respectively. The weak π – π stacking and C–H··· π interactions make a small contribution to the HF surface, with C–C contacts having a value of 9.5% for both compounds, as expected. Dispersion and other van der Waals forces are also important in the formation of the solid with H–C/C–H contacts constituting 15.5% of the HF map. The high proportion of non-bonded H–H (41.6–41.7% in both compounds) contacts suggests a considerable contribution of long-range hydrophobic interactions represented by the blue region. Figure 5d displays the electrostatic potential mapped over the HF surface, showing the positive potential in blue representing the hydrogen donor regions and the negative potential in red indicating the acceptor

fragments of the molecules. 2D (two-dimensional) full fingerprint plots for **5** and **6** are shown in Fig. 5e, f, respectively. The similarity in the plots indicates equal intermolecular interactions for the two compounds.

Energy models of interactions between molecules in the construction of the crystals were analyzed by taking Co(II) complex **6** as a reference, considering its similar supramolecular structure to **5**. These interactions were calculated using the HF/3-21G energy model implemented in Crystal Explorer (Turner et al. 2017), which uses quantum mechanical charge distributions for unperturbed molecules (Mackenzie et al. 2017). In these calculations, the total interaction energy is modeled as the sum of the electrostatic (E_{ele}), polarization (E_{pol}), dispersion (E_{dis}) and exchange–repulsion (E_{rep}) terms. In Table 3, the interaction energies for selected molecular pairs in the first coordination sphere around the asymmetric unit are summarized. By observing the results, it is possible to deduce that despite the high contribution from strong C–H···O interactions, the dispersion terms contribute the greatest proportion to the total energy in the crystal structure. The strongest pairwise interaction, with a total energy of -136.8 kJ mol⁻¹, corresponds to the molecules joined by strong O1–H1–O3(B, A) hydrogen bonds along the [100] direction involving water molecules in the connections (Figs. 5b, 6a). Figure 6b–d show the energy framework diagrams for pairs of molecules for separate, electrostatic (red) and dispersion (green) contributions to the total nearest-neighbor pairwise interaction energies (blue). As observed, the cylinders serve as a guide that connects molecular centroids and their respective thicknesses represent the relative magnitude of the energy. The energy framework diagrams for pairs of molecules suggest an anisotropic topology of sheets stacked along the [010] as observed previously in the intermolecular hydrogen bond interactions.

DFT calculations

With the purpose of investigating further the proposed structures of metal complexes with **L1**, from which unfortunately we could not obtain crystals, we carried out DFT calculations. The model system used in the DFT study was M–**L1** with M=Co, Cu, Ni, Zn. The results of the calculations indicate that the metal

Table 3 CE–HF interaction energies (kJ mol^{-1} ; $1 \text{ kJ mol}^{-1}=0.239 \text{ kcal mol}^{-1}$) for complex **6**

N	Symop	R	E_{ele}	E_{pol}	E_{dis}	E_{rep}	E_{tot}
1	$-x, -y, -z$	13.80	-10.2	-4.9	-14.0	5.1	-22.0
1	$-x+1/2, y+1/2, -z+1/2$	13.69	-4.7	-2.7	-12.9	3.2	-15.6
1	$-1/2+x, 1/2-y, -1/2+z$	7.45	-82.5	-30.3	-127.5	100.8	-136.8

N is the number of molecules with an R molecular centroid-to-centroid distance (\AA)

Electron density was calculated using HF/3-21G model energies

Note scale factors used to determine E_{tot} : $E_{\text{ele}}=1.019$, $E_{\text{pol}}=0.651$, $E_{\text{dis}}=0.901$ and $E_{\text{rep}}=0.811$

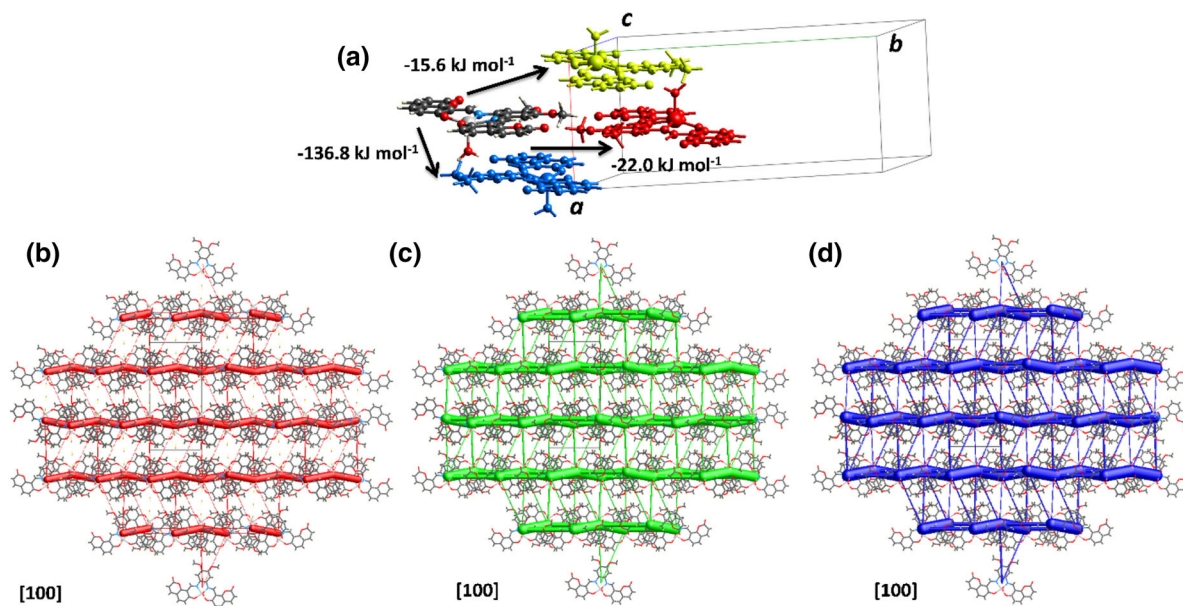


Fig. 6 a Graphical representation of CE–HF interaction energies (kJ mol^{-1}) for **6**. Energy-framework diagrams for **b** electrostatic (red) and **c** dispersion (green) contributions to **d** the total interaction energies (blue) in complex **6**. (Color figure online)

center ($M=\text{Co, Cu, Ni, Zn}$) and the four atoms coordinating it (N1, N2, O1 and O2 , Fig. S47) are all lying in the same plane (dihedral O1-M-N1-N2 ranges from 177.5° to 180°). The phenyl and the coumarin groups are almost perfectly coplanar when $M=\text{Cu, Ni}$, ranging the dihedral O1-M-C1-C2 between 0.5° and 2.7° and slightly staggered when $M=\text{Co, Zn}$, being dihedral O1-M-C1-C2 23.7° and 16.5° respectively (see Fig. S47). This different behavior is also reflected in the distances $M\text{-O1}$ and $M\text{-N1}$, which are almost identical when $M=\text{Cu, Ni}$, whereas are different when $M=\text{Co, Zn}$ ($\text{Zn-O1}=2.05 \text{ \AA}$, $\text{Zn-N1}=1.93 \text{ \AA}$ and $\text{Co-O1}=2.06 \text{ \AA}$, $\text{Co-N1}=1.88 \text{ \AA}$).

Cell viability assay

The treatment of complexes (**1–9**) and ligands (**L₁** and **L₂**) was performed at various concentrations (10, 30, 40, 50, 70, and $100 \mu\text{M}$). The IC_{50} values are presented in Table 4, these results were obtained after a non-linear adjustment from dose–response curve of percent viability versus the test concentration of each compound. Potential anticarcinogenic activity is attributed to compounds that exhibit low toxic effects on the normal cell lines (HFF-1 and HaCaT) and high cytotoxicity against the carcinoma cell line (HeLa) (Ali et al. 2016). Our results showed that the Zn(II) , Cu(II) , Ni(II) and Pt(II) complexes (**1, 4, 5, 7, 8** and **9**) did not exhibit selective cytotoxicity effect on

Table 4 IC₅₀ values for L₁, L₂ and metal complexes 1–10 toward the carcinogenic cell line HeLa and the non-carcinogenic cell lines HFF and HaCaT

Compound	IC ₅₀ (μM)		
	HeLa	HFF-1	HaCaT
L ₁	9.6±2.6	2.9±1.7	61.3±4.5
1	86.9±9.0	60.6±6.4	11.4±2.2
2	3.5±1.2	12.0±0.6	2.0±1.2
3	52.5±1.0	83.3±5.9	74.9±1.3
4	72.7±8.1	3.0±2.2	66.4±0.3
L ₂	36.9±6.7	61.9±7.9	62.4±4.1
5	90.7±2.5	81.5±5.4	54.3±5.8
6	4.1±0.9	17.6±5.2	9.3±1.7
7	83.5±4.7	66.5±4.7	99.0±7.7
8	85.1±1.6	77.5±2.2	87.6±6.1
9	61.4±1.1	1.8±0.6	50.5±6.1
Cisplatin	11.6±2.7	84.8±4.8	7.8±2.1

HeLa human cervical cancer cells, *HFF-1* human foreskin fibroblast cells, *HaCaT* human keratinocytes

HeLa cells, instead they exhibited similar or higher cytotoxicity against HaCaT, HFF-1, or both cell lines (Table 4). However, complexes **5**, **7** and **8** presented low cytotoxicity against HFF-1 and HaCaT cells; therefore, it would be interesting to test their cytotoxicity against other commonly used carcinogenic cell lines, such as adenocarcinoma human alveolar basal epithelial cells (A549), human liver hepatocellular carcinoma cells (HepG-2) and human breast cancer cells (MCF 7) (Cindrić et al. 2017; Tabrizi et al. 2017; Gomathi and Selvameena 2018).

Interestingly, **3** and the ligand L₂ exhibited appreciable potential anticarcinogenic activity due to their high cytotoxicity against HeLa cells compared to HFF-1 and HaCaT cells (Table 4). This activity might be influenced by the presence or lack of the structural modification (-OMe groups). For instance, in contrast to L₂, L₁ did not present anticarcinogenic potential (i.e., it exhibited high cytotoxicity against not only HeLa cells but also to HFF-1 cells). Similarly, Cu(II) complex **3** presented anticarcinogenic potential, while the Cu(II) complex **8** showed no potential. Nevertheless, to elucidate the exact structure–activity relation, further mechanistic studies must be performed.

Among all the evaluated compounds, Co(II) complexes **2** and **6** exhibited the highest cytotoxicity against HeLa cells and thus the highest

anticarcinogenic potential. It has been demonstrated that Co(II) complexes may also act through an oxidative stress mechanism due to their known dynamic redox activity (Jungwirth et al. 2011; Kochem et al. 2012a, 2012b). These results might be explained as HeLa cells have much lower glutathione (GSH) levels than HaCaT cells (Tipnis et al. 1999; Mukherjee et al. 2012). GSH plays an important role in the antioxidant and reactive oxygen species (ROS) scavenging cell response. Therefore, under oxidative stress conditions, HeLa cells will exhibit higher ROS production than HaCaT cells, which consequently will trigger cell death (Mukherjee et al. 2012).

On the other hand, compared to cisplatin, Co(II) complex **6** showed lower cytotoxic effects on the normal HaCaT cells, while both complexes **2** and **6** exhibited higher activity towards HeLa cells (Table 4). This result allowed us to suggest that these complexes may exert a better anticarcinogenic potential than cisplatin. Additionally, **2** and **6** also present a better potential than a reported Co(II) salen complex whose IC₅₀ values against HeLa and HFF cells were 8±2 μM and 23±2 μM, respectively (Ali et al. 2016). As far as we are concerned, complexes **2** and **6** are one of the first salen Co(II) complexes reported to present anticarcinogenic potential. Additionally, the square-pyramidal geometry of **6**, as

indicated by X-ray crystallography, along with all the chemical properties of the ligand and the metallic center described before, suggests that one of the probable mechanisms of their anticarcinogenic action could be the stabilization of the G4 DNA structure. As there is no evidence of this mechanism, further mechanistic studies are being carried out by our group. In general, this study demonstrates salphen-type complexes that exhibit anticarcinogenic activity.

Molecular dynamics calculations

In recent years, studies on DNA G4 helices interacting with salphen compounds have led to the elucidation of the binding pose by means of X-ray crystallography (Campbell et al. 2012). This facilitates performing classical molecular dynamics (MD) simulations as it offers a reliable initial configuration. We performed MD simulations with scope of shedding light on the plasticity of the system as well as the most conserved interactions over time. Here, we simulated seven systems: ligands **L**₁ and **L**₂ bound to the G4 quadruplex at different protonation states (**L**₁, **L**₂, **HL**₁, and **HL**₂) or in complex with Co(II) (**2** and **6**) and the **APO** structure of the G4 helix (see the Materials and Methods section for details). It is important to note that, from a molecular-mechanical stand, the only difference between various coordination complexes is the bonded parameters internal of the molecule and the van der Waals radius of the metal. Thus, for the sake of accuracy, the metallic architectures **2** and **6** will be hereafter referred to as the generic **ML**₁ and **ML**₂, respectively.

Firstly, the dynamic stability of the DNA was studied in the various systems to corroborate that its geometry remains similar to that found in the original crystal structure (pdb code 3QSC (Campbell et al. 2012)). As it can be seen from Fig. S48, the root-mean squared deviation (RMSD) of the nucleic acids oscillates between 3 and 6 Å, indicating a high mobility of the quadruplex. However, when the terminal pairs are excluded from the calculation, the RMSD quickly drops to an acceptable range of 1 – 2.5 Å (Fig. 7a top). As expected, this indicates that the terminal bases of the quadruplex, that is those with the highest solvent accessible surface area, are the ones with the highest fluctuations along the simulations. Similarly, the same metric was calculated for the bound ligands in our holo conformations

(Fig. 7a middle). Interestingly, **ML**₁ and **ML**₂ are the two most stable systems maintaining a nearly constant RMSD of less than 0.5 Å and staying stacked between the nitrogenous bases during the entirety of the simulations. In contrast, the other four studied ligands display a higher flexibility. To identify the source of the increased RMSD for ligands **L**₁, **L**₂, **HL**₁, and **HL**₂, the torsion angles between the terminal coumarin heterocycles and the central phenyl ring were computed. The bottom of Fig. 7a shows the distribution of one of these angles over time, whilst the second one can be found in Fig. S49. As seen from Fig. 7a, there is a correlation between the RMSD and the torsion angles, suggesting that the planarity of the non-metallic compounds is exchanged for more favorable interactions with the DNA.

Based on these results, we proceeded to describe the interactions that drive the binding of the studied compounds onto a G4 helix. For this, the structure of the compounds was first divided into three regions (Fig. 7b): the two coumarin rings, namely the left-hand side (LHS) and the right-hand side (RHS), and the central aromatic ring (LINK). The lifetime of the available contacts was calculated and plotted as a heat map in Fig. 7c. This graph corroborates that **ML**₁ and **ML**₂ are the most static compounds once bound to the quadruplex. **ML**₁ and **ML**₂ both present conserved interactions between LHS/DG-4 and LINK/DG-10'. The RHS, instead, displays an interchange between DG-4' and DG-10. Notably, the upper terminal bases DT3-11 and DT3-11' anchor less often to the ligands likely due to the entropic contributions of their interactions with the solvent. Furthermore, none of the studied compounds shows interactions as conserved as the ones by **ML**₁ and **ML**₂. Moreover, when scrutinizing the contacts displayed by **ML**₁ and **ML**₂ we find a substantial difference. In **ML**₁, the metal atom remains in the vicinity of the thiamine residues for 55% of the simulation (i.e. 45% with DT3-11' and 10% with DT3-11), whereas, in **ML**₂, this value is reduced to only 29% (always with DT3-11'). This is likely due to the additional steric stress introduced by the extra methyl substituents in **ML**₂. In summary, our MD simulations reveal that the coordination compounds **ML**₁ and **ML**₂ represent the most dynamically stable systems in complex with G4-quadruplexes as

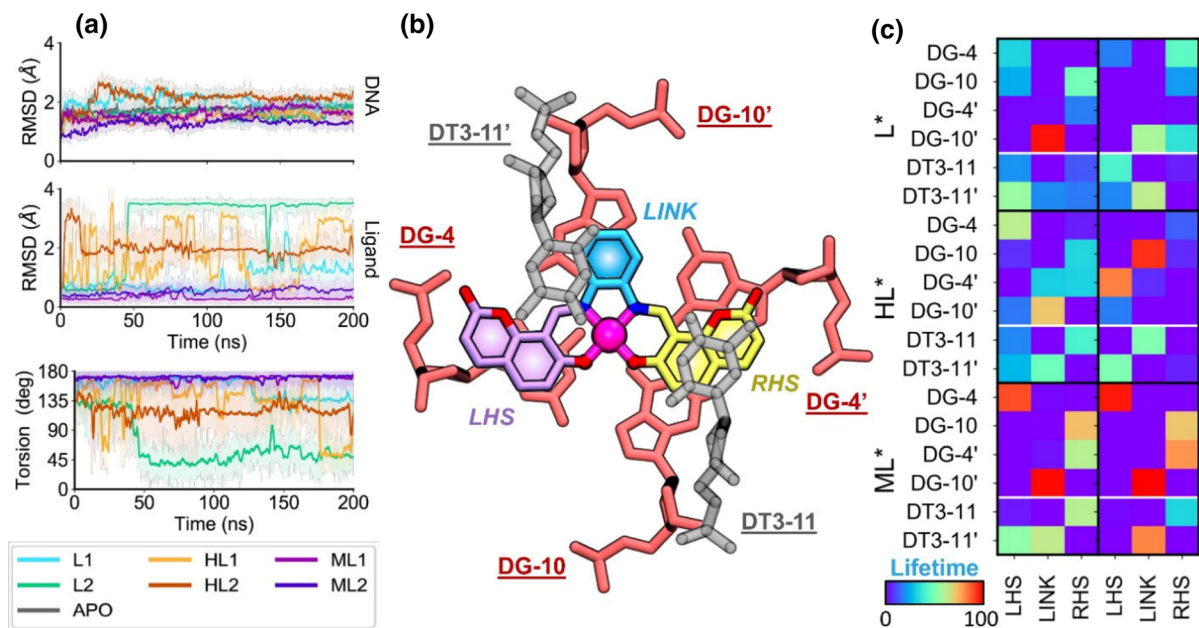


Fig. 7 **a** Dynamic features of the seven simulations performed. Root-mean-squared deviation (RMSD) of the internal nucleic acids (top) and the bound ligands (middle). Torsion angle formed between a coumarin cycle and the central ring

contrasted by the uncoordinated ligands **L**₁, **L**₂, **HL**₁, and **HL**₂.

Conclusion

In summary, one new coumarin salphen ligand was synthesized (**L**₂) and fully characterized. Using the previously reported ligand **L**₁ and the novel ligand **L**₂, eight new complexes of Zn(II), Co(II), Cu(II), Ni(II) and Pt(II) (**2–9**) were obtained. These complexes were characterized by spectroscopic, elemental and TGA techniques. The analyses and spectral data showed that complexes **2–9** had a metal-to-ligand ratio (M:L) of 1:1 and the coordination of a water ligand to complexes **2–8** was proposed. Additionally, the Zn(II), Co(II), Cu(II), and Ni(II) complexes showed higher thermal stability than Pt(II) complex **9**. Furthermore, the crystal structures of complexes **5** and **6** demonstrated a square-pyramidal geometry with a molecule of water as an axial ligand. A cytotoxicity assay showed that among all the evaluated compounds, Co(II) complexes **2** and **6** presented the highest anticarcinogenic potential, and also presented better activity than cisplatin on HeLa cells.

(bottom). **b** Graphical representation of the bound ligands and the proximal nitrogenous bases. **c** Contact map between the bound ligands and the vicinal nucleic acids. (Color figure online)

According to MD simulations, the Co(II) complexes display better-conserved contacts with the last guanine quartet and the terminal thymine bases of G4 as compared to the free ligands **L**₁ and **L**₂, which is in good agreement with their increased activity observed in the in vitro assessment. Studies to further elucidate their structure–activity relationship are in progress.

Acknowledgements The authors thank the Departamento de Química, Facultad de Ciencias and Vicerrectoría de Investigaciones of the Universidad de los Andes for financial support (project no. INV-2018-50-1354). The authors would also like to thank Camilo Andrés Ortiz Casas for his assistance with the viability data processing. Gian Pietro Miscione, Mario A. Macías and Sebastián Franco-Ulloa would like to acknowledge the High- Performance Computing Center of the Universidad de los Andes, Bogotá (Colombia) for the computational resources and the “Fondo de Apoyo para Profesores Asistentes” of the same institution for financial support.

References

- Abd Karim NH, Mendoza O, Shivalingam A et al (2014) Salphen metal complexes as tunable G-quadruplex

- binders and optical probes. *RSC Adv* 4:3355–3363. <https://doi.org/10.1039/C3RA44793F>
- Addison AW, Rao TN, Reedijk J et al (1984) Synthesis, structure, and spectroscopic properties of copper(II) compounds containing nitrogen–sulphur donor ligands; the crystal and molecular structure of aqua[1,7-bis(N-methylbenzimidazol-2'-yl)-2,6-dithiaheptane]copper(II) perchlorate. *J Chem Soc, Dalton Trans.* <https://doi.org/10.1039/DT9840001349>
- Akbari A, Alinia Z (2013) Comparative Analysis of the Ni(II) Complex of the N, N'-Bis-(4-Hydroxysalicylidene)-1, 2-Diaminoethane: combined experimental and theoretical study (DFT/PW91). *Comput Res* 1:19–26. <https://doi.org/10.13189/cr.2013.010201>
- Ali A, Kamra M, Bhan A et al (2016) New Fe(III) and Co(II) salen complexes with pendant distamycins: selective targeting of cancer cells by DNA damage and mitochondrial pathways. *Dalt Trans* 45:9345–9353. <https://doi.org/10.1039/C5DT04374C>
- Allendorf MD, Bauer CA, Bhakta RK, Houk RJT (2009) Luminescent metal–organic frameworks. *Chem Soc Rev* 38:1330. <https://doi.org/10.1039/b802352m>
- Andrae D, Haussermann U, Dolg M et al (1990) Energy-adjusted ab initio pseudopotentials for the second and third row transition elements. *Theor Chim Acta* 77:123–141. <https://doi.org/10.1007/BF01114537>
- Aranha PE, dos Santos MP, Romera S, Dockal ER (2007) Synthesis, characterization, and spectroscopic studies of tetradentate Schiff base chromium(III) complexes. *Polyhedron* 26:1373–1382. <https://doi.org/10.1016/j.poly.2006.11.005>
- Balzani V, Bergamini G, Campagna S, Puntoriero F (2007) Photochemistry and photophysics of coordination compounds: overview and general concepts. *Photochemistry and photophysics of coordination compounds I*. Springer-Verlag, Berlin Heidelberg, pp 1–36
- Bayly CI, Cieplak P, Cornell WD, Kollman PA (1993) A well-behaved electrostatic potential based method using charge restraints for deriving. *J Phys Chem* 97:10269–10280. <https://doi.org/10.1021/j100142a004>
- Borthakur R, Kumar A, De AK, Lal RA (2015) Synthesis, characterization and electrochemical properties of copper (II) complexes derived from succinoyldihydrazine Schiff base ligands. *Arab J Chem.* <https://doi.org/10.1016/j.arabjc.2014.12.040>
- Bottoni A, Calvaresi M, Ciogli A et al (2013) Selective and practical oxidation of sulfides to diastereopure sulfoxides: a combined experimental and computational investigation. *Adv Synth Catal* 355:191–202. <https://doi.org/10.1002/adsc.201200459>
- Bray F, Ferlay J, Soerjomataram I et al (2018) Global cancer statistics 2018: GLOBOCAN estimates of incidence and mortality worldwide for 36 cancers in 185 countries. *CA Cancer J Clin* 33:2597–2604. <https://doi.org/10.3322/caac.21492>
- Burge S, Parkinson GN, Hazel P et al (2006) Quadruplex DNA: sequence, topology and structure. *Nucleic Acids Res* 34:5402–5415. <https://doi.org/10.1093/nar/gkl655>
- Campbell NH, Karim NHA, Parkinson GN et al (2012) Molecular basis of structure-activity relationships between salphen metal complexes and human telomeric DNA quadruplexes. *J Med Chem* 55:209–222. <https://doi.org/10.1021/jm201140v>
- Cao Q, Li Y, Freisinger E et al (2017) G-quadruplex DNA targeted metal complexes acting as potential anticancer drugs. *Inorg Chem Front* 4:10–32. <https://doi.org/10.1039/c6qi00300a>
- Carvalho ATP, Teixeira AFS, Ramos MJ (2013) Parameters for molecular dynamics simulations of iron-sulfur proteins. *J Comput Chem* 34:1540–1548. <https://doi.org/10.1002/jcc.23287>
- Castillo KF, Bello-Vieda NJ, Nuñez-Dallos NG et al (2016) Metal complex derivatives of azole: a study on their synthesis, characterization, and antibacterial and antifungal activities. *J Braz Chem Soc* 27:2334–2347. <https://doi.org/10.5935/0103-5053.20160130>
- Cindrić M, Bjelopetrović A, Pavlović G et al (2017) Copper(II) complexes with benzhydrazone-related ligands: synthesis, structural studies and cytotoxicity assay. *New J Chem* 41:2425–2435. <https://doi.org/10.1039/C6NJ03827A>
- Darden T, York D, Pedersen L (1993) Particle mesh Ewald: An N log(N) method for Ewald sums in large systems. *J Chem Phys* 98:10089–10092. <https://doi.org/10.1063/1.464397>
- Datta S, Mahapatra AS, Sett P et al (2018) Magnetic measurements, Raman and infrared spectra of metal – ligand complex derived from CoCl₂ · 6H₂O and 2-benzoyl pyridine. *Bull Mater Sci* 41:1–10. <https://doi.org/10.1007/s12034-018-1560-z>
- David AP, Margarit E, Domizi P et al (2016) G-quadruplexes as novel cis-elements controlling transcription during embryonic development. *Nucleic Acids Res* 44:4163–4173. <https://doi.org/10.1093/nar/gkw011>
- Dogaheh SG, Heras Ojea MJ, Piquer LR et al (2016) CoII and CuII fluorescent complexes with acridine-based ligands. *Eur J Inorg Chem* 2016:3314–3321. <https://doi.org/10.1002/ejic.201600297>
- Frisch MJ, Trucks GW, Schlegel HB et al (2016) Gaussian 16 {R}evision {C}.01. Gaussian, Inc., Wallingford, CT
- Giacinto P, Bottoni A, Calvaresi M, Zerbetto F (2014) Cl[−] Exchange S_N2 Reaction inside Carbon Nanotubes: C–H⋯π and Cl⋯π Interactions Govern the Course of the Reaction. *J Phys Chem C* 118:5032–5040. <https://doi.org/10.1021/jp412456q>
- Giacinto P, Cera G, Bottoni A et al (2015) DFT Mechanistic Investigation of the Gold(I)-Catalyzed Synthesis of Azepero[1,2- a]indoles. *ChemCatChem* 7:2480–2484. <https://doi.org/10.1002/cctc.201500429>
- Gomathi V, Selvameena R (2018) Spectroscopic investigation, fluorescence quenching, in vitro antibacterial and cytotoxicity assay of Co(II) and Ni(II) complexes containing 4-((3-ethoxy-2-hydroxy benzylidene)amino)-N-(pyridin-2-yl)benzenesulfonamide. *Inorganica Chim Acta* 480:42–46. <https://doi.org/10.1016/j.ica.2018.05.007>
- Hänsel-Hertsch R, Di Antonio M, Balasubramanian S (2017) DNA G-quadruplexes in the human genome: detection, functions and therapeutic potential. *Nat Rev Mol Cell Biol* 18:279–284. <https://doi.org/10.1038/nrm.2017.3>
- Hartering CG, Nazarov A, Ashraf SM, et al (2008) Carbohydrate-metal complexes and their potential as anticancer agents. *Curr Med Chem* 15:2574–2591. <https://doi.org/10.2174/092986708785908978>

- Hassan AY, Sarg MT, El Deeb MA et al (2018) Facile synthesis and anticancer activity study of novel series of substituted and fused coumarin derivatives. *J Heterocycl Chem* 55:1426–1443. <https://doi.org/10.1002/jhet.3179>
- Hess B, Bekker H, Berendsen HJC, Fraaije JGEM (1997) LINCS: A linear constraint solver for molecular simulations. *J Comput Chem* 18:1463–1472. [https://doi.org/10.1002/\(SICI\)1096-987X\(199709\)18:12%3c1463::AID-JCC4%3e3.0.CO;2-H](https://doi.org/10.1002/(SICI)1096-987X(199709)18:12%3c1463::AID-JCC4%3e3.0.CO;2-H)
- Houjou H, Yagi K, Yoshikawa I et al (2017) Effects of interaction between the chelate rings and π -conjugated systems in fused salphen complexes on UV-Vis-NIR spectra. *J Phys Org Chem* 30:e3635. <https://doi.org/10.1002/poc.3635>
- Ivani I, Dans PD, Noy A et al (2015) Parmbsc1: a refined force field for DNA simulations. *Nat Methods* 13:55–58. <https://doi.org/10.1038/nmeth.3658>
- Jayatilaka D, Grimwood DJ, Lee A et al (2005) TONTO. University of Western Australia, Perth
- Jones RN, Angell CL, Smith J (1959) The carbonyl stretching bands in the infrared spectra of unsaturated lactones. *Can J Chem* 37:2007–2022
- Jorgensen WL, Chandrasekhar J, Madura JD et al (1983) Comparison of simple potential functions for simulating liquid water. *J Chem Phys* 79:926. <https://doi.org/10.1063/1.445869>
- Jungwirth U, Kowol CR, Keppler BK et al (2011) Anticancer activity of metal complexes: involvement of redox processes. *Antioxid Redox Signal* 15:1085–1127. <https://doi.org/10.1089/ars.2010.3663.Anticancer>
- Kajal A, Bala S, Kamboj S et al (2013) Schiff Bases: A Versatile Pharmacophore. *J Catal* 2013:1–14. <https://doi.org/10.1155/2013/893512>
- Kavitha N, Anantha Lakshmi PV (2017) Synthesis, characterization and thermogravimetric analysis of Co(II), Ni(II), Cu(II) and Zn(II) complexes supported by ONNO tetradentate Schiff base ligand derived from hydrazino benzoxazine. *J Saudi Chem Soc* 21:S457–S466. <https://doi.org/10.1016/j.jscs.2015.01.003>
- Kilic A, Koyuncu I, Durgun M et al (2018) Synthesis and Characterization of the Hemi-Salen Ligands and Their Triboron Complexes: Spectroscopy and Examination of Anticancer Properties. *Chem Biodivers* 15:1–13. <https://doi.org/10.1002/cbdv.201700428>
- Kochem A, Chiang L, Baptiste B et al (2012) Ligand-Centered Redox Activity in Cobalt(II) and Nickel(II) Bis(phenolate)-Dipyrrin Complexes. *Chem A Eur J* 18:14590–14593. <https://doi.org/10.1002/chem.201202882>
- Kochem A, Kanso H, Baptiste B et al (2012) Ligand contributions to the electronic structures of the oxidized cobalt (II) salen complexes. *Inorg Chem* 51:10557–10571. <https://doi.org/10.1021/ic300763t>
- Larkin PJ (2018a) IR and Raman Spectra-Structure Correlations. *Infrared and Raman Spectroscopy*, 2nd edn. Elsevier, Cambridge, pp 85–134
- Larkin PJ (2018b) Introduction: Infrared and Raman Spectroscopy. *Infrared and Raman Spectroscopy*, 2nd edn. Elsevier, Cambridge, pp 1–5
- Ma D-L, Pui-Yan V, Leung K et al (2013) Structure-Based Approaches Targeting Oncogene Promoter G-Quadruplexes. In: Siregar Y (ed) *Oncogene and Cancer-From Bench to Clinic*. Inst za onkologiju i radio, USA, pp 131–150
- Mackenzie CF, Spackman PR, Jayatilaka D, Spackman MA (2017) CrystalExplorer model energies and energy frameworks: extension to metal coordination compounds, organic salts, solvates and open-shell systems. *IUCrJ* 4:575–587. <https://doi.org/10.1107/S205225251700848X>
- Macrae CF, Bruno IJ, Chisholm JA et al (2008) Mercury CSD 2.0 – new features for the visualization and investigation of crystal structures. *J Appl Crystallogr* 41:466–470. <https://doi.org/10.1107/S0021889807067908>
- Mehmood RK (2014) Review of cisplatin and oxaliplatin in current immunogenic and monoclonal antibodies perspective. *Oncol Rev* 8:36–43. <https://doi.org/10.4081/oncol.2014.256>
- Mendoza O, Bourdoncle A, Boulé J et al (2016) G-quadruplexes and helicases. *Nucleic Acids Res* 44:1989–2006. <https://doi.org/10.1093/nar/gkw079>
- Mukherjee SG, O’Clonadh N, Casey A, Chambers G (2012) Comparative in vitro cytotoxicity study of silver nanoparticle on two mammalian cell lines. *Toxicol Vitro* 26:238–251. <https://doi.org/10.1016/j.tiv.2011.12.004>
- Nakamoto K (2008) *Applications in Coordination Chemistry. Infrared and Raman Spectra of inorganic and coordination compounds: part B: applications in coordination, organometallic, and bioinorganic chemistry*. Sixth. John Wiley & Sons Inc, New Jersey, pp 7–10
- Nuñez-Dallos N, Cuadrado C, Hurtado J et al (2016) In situ-Mercury Film Electrode for Simultaneous Determination of Lead and Cadmium Using Nafion Coated New Coumarin Schiff Base as Chelating-Adsorbent. *Int J Electrochem Sci* 11:9855–9867. <https://doi.org/10.20964/2016.12.02>
- Nuñez-Dallos N, Posada AF, Hurtado J (2017) Coumarin salen-based zinc complex for solvent-free ring opening polymerization of ϵ -caprolactone. *Tetrahedron Lett* 58:977–980. <https://doi.org/10.1016/j.tetlet.2017.01.088>
- Parrinello M, Rahman A (1981) Polymorphic transitions in single crystals: A new molecular dynamics method. *J Appl Phys* 52:7182–7190. <https://doi.org/10.1063/1.328693>
- Pérez A, Marchán I, Svozil D et al (2007) Refinement of the AMBER force field for nucleic acids: improving the description of alpha/gamma conformers. *Biophys J* 92:3817–3829. <https://doi.org/10.1529/biophysj.106.097782>
- Reed JE, Arnal AA, Neidle S, Vilar R (2006) Stabilization of G-quadruplex DNA and inhibition of telomerase activity by square-planar nickel(II) complexes. *J Am Chem Soc* 128:5992–5993. <https://doi.org/10.1021/ja058509n>
- Robillard MS, Reedijk J (2011) Platinum-Based Anticancer Drugs. In: Scott RA (ed) *Encyclopedia of Inorganic and Bioinorganic Chemistry*. Wiley, Chichester, UK
- Schweitzer G, Pesterfeld L (2010) The Ti Group and the 5B, 6B, 7B and 8B Heavy elements. *The Aqueous Chemistry of the Elements*. Oxford University Press Inc, New York, pp 330–333
- Seminario JM (1996) Calculation of intramolecular force fields from second-derivative tensors. *Int J Quantum Chem* 60:1271–1277. [https://doi.org/10.1002/\(SICI\)1097-461X\(1996\)60:7%3c1271::AID-QUA8%3e3.0.CO;2-W](https://doi.org/10.1002/(SICI)1097-461X(1996)60:7%3c1271::AID-QUA8%3e3.0.CO;2-W)

- Sharma V, Arora EK, Cardoza S (2016) Synthesis, antioxidant, antibacterial, and DFT study on a coumarin based salen-type Schiff base and its copper complex. *Chem Pap* 70:1493–1502. <https://doi.org/10.1515/chempap-2016-0083>
- Sheldrick GM (2015) Crystal structure refinement with SHELXL. *Acta Crystallogr Sect C Struct Chem* 71:3–8. <https://doi.org/10.1107/S2053229614024218>
- Socrates G (2004) Infrared and Raman characteristic group frequencies. Tables and charts, 3rd edn. Wiley, West Sussex
- Spackman MA, McKinnon JJ, Jayatilaka D (2008) Electrostatic potentials mapped on Hirshfeld surfaces provide direct insight into intermolecular interactions in crystals. *CrystEngComm* 10:377–388. <https://doi.org/10.1039/b715227b>
- Suffren Y, Rollet F-G, Reber C (2012) Raman spectroscopy of transition metal complexes: Molecular vibrational frequencies, phase transitions, isomers and electronic structure. *Comments Inorg Chem A J Crit Discuss Curr Lit* 32:246–276. <https://doi.org/10.1080/02603594.2012.659776>
- Tabrizi L, Talaie F, Chiniforoshan H (2017) Copper(II), cobalt (II) and nickel(II) complexes of lapachol: synthesis, DNA interaction, and cytotoxicity. *J Biomol Struct Dyn* 35:3330–3341. <https://doi.org/10.1080/07391102.2016.1254118>
- Tipnis SR, Blake DG, Shepherd AG, McLellan LI (1999) Overexpression of the regulatory subunit of gamma-glutamylcysteine synthetase in HeLa cells increases gamma-glutamylcysteine synthetase activity and confers drug resistance. *Biochem J* 337:559–566
- Turner MJ, McKinnon JJ, Wolff SK et al (2017) *CrystalExplorer17*. University of Western Australia, Perth
- Voulgari E, Bakandritsos A, Galtsidis S et al (2016) Synthesis, characterization and in vivo evaluation of a magnetic cisplatin delivery nanosystem based on PMAA-graft-PEG copolymers. *J Control Release* 243:342–356. <https://doi.org/10.1016/j.jconrel.2016.10.021>
- Wang J, Cieplak P, Kollman PA (2000) How well does a restrained electrostatic potential (RESP) model perform in calculating conformational energies of organic and biological molecules? *J Comput Chem* 21:1049–1074. [https://doi.org/10.1002/1096-987X\(200009\)21:12%3c1049::AID-JCC3%3e3.0.CO;2-F](https://doi.org/10.1002/1096-987X(200009)21:12%3c1049::AID-JCC3%3e3.0.CO;2-F)
- Wang J, Wolf RM, Caldwell JW et al (2004) Development and testing of a general amber force field. *J Comput Chem* 25:1157–1174. <https://doi.org/10.1002/jcc.20035>
- Winston A, Kemper N (1971) The split carbonyl band in the infrared spectra of halogen derivatives of 4-hydroxy-2,4-pentadienoic acid lactone. *Tetrahedron* 27:543–548. <https://doi.org/10.1177/0892705707073082>
- Wolff SK, Grimwood DJ, McKinnon JJ et al (2012) *Crystal Explorer 3.1*. University of Western Australia, Perth
- Wu P, Ma DL, Leung CH et al (2009) Stabilization of G-quadruplex DNA with platinum(II) Schiff base complexes: Luminescent probe and down-regulation of c-myc oncogene expression. *Chem - A Eur J* 15:13008–13021. <https://doi.org/10.1002/chem.200901943>
- Xie LX, Zheng XF, Li X et al (2008) Structures, fluorescent properties of the d10 metal ions compounds based on molecular clips. *Synth React Inorganic, Met Nano-Metal Chem* 38:591–597. <https://doi.org/10.1080/15533170802293253>
- Yang W, Chen X, Su H et al (2015) The fluorescence regulation mechanism of the paramagnetic metal in a biological HNO sensor. *Chem Commun* 51:9616–9619. <https://doi.org/10.1039/C5CC00787A>
- Zhao Y, Tishchenko O, Truhlar DG (2005) How Well Can Density Functional Methods Describe Hydrogen Bonds to π Acceptors? *J Phys Chem B* 109:19046–19051. <https://doi.org/10.1021/jp0534434>
- Zhao Y, Truhlar DG (2004) Hybrid Meta Density Functional Theory Methods for Thermochemistry, Thermochemical Kinetics, and Noncovalent Interactions: The MPW1B95 and MPWB1K Models and Comparative Assessments for Hydrogen Bonding and van der Waals Interactions. *J Phys Chem A* 108:6908–6918. <https://doi.org/10.1021/jp048147q>
- Zhao Y, Truhlar DG (2005) Design of Density Functionals That Are Broadly Accurate for Thermochemistry, Thermochemical Kinetics, and Nonbonded Interactions. *J Phys Chem A* 109:5656–5667. <https://doi.org/10.1021/jp050536c>
- Zhao Y, Truhlar DG (2008) Density Functionals with Broad Applicability in Chemistry. *Acc Chem Res* 41:157–167. <https://doi.org/10.1021/ar700111a>

Publisher's Note Springer Nature remains neutral with regard to jurisdictional claims in published maps and institutional affiliations.